

## Potential field migration for rapid imaging of gravity gradiometry data

Michael S. Zhdanov<sup>1,2\*</sup>, Xiaojun Liu<sup>2</sup>, Glenn A. Wilson<sup>1</sup> and Le Wan<sup>2</sup>

<sup>1</sup>TechnoImaging, 4001 South, 700 East, Suite 500, Salt Lake City, UT 84107, USA, and <sup>2</sup>Department of Geology and Geophysics, The University of Utah, Frederick Albert Sutton Building 115, 1460 East Room 383, Salt Lake City, UT 84112, USA

Received: December 2010, revision accepted: July 2011

### ABSTRACT

The geological interpretation of gravity gradiometry data is a very challenging problem. While maps of different gravity gradients may be correlated with geological structures present, maps alone cannot quantify 3D density distributions related to geological structures. 3D inversion represents the only practical tool for the quantitative interpretation of gravity gradiometry data. However, 3D inversion is a complicated and time-consuming procedure that is very dependent on the a priori model and constraints used. To overcome these difficulties for the initial stages of an interpretation workflow, we introduce the concept of potential field migration, and demonstrate how it can be applied for rapid 3D imaging of entire gravity gradiometry surveys. This method is based on a direct integral transformation of the observed gravity gradients into a subsurface density distribution that can be used for interpretation or as an a priori model for subsequent 3D regularized inversion. For large-scale surveys, we show how migration runs on the order of minutes compared to hours for 3D regularized inversion. Moreover, the results obtained from potential field migration are comparable to those obtained from regularized inversion with smooth stabilizers. We present a case study for the 3D imaging of FALCON airborne gravity gradiometry data from Broken Hill, Australia. We observe good agreement between results obtained from potential field migration and those generated by 3D regularized inversion.

**Key words:** Gradiometry, Gravitation, Migration.

### INTRODUCTION

All targeting decisions pertaining to hydrocarbon exploration are based on geological interpretations of depth-converted seismic data. For salt and basalt plays, an accurate depth conversion workflow needs to include both 3D velocity and density models. Given the non-uniqueness of recovering both the velocity and density from acoustic impedance, independent measures of the subsurface density are essential. As in mineral exploration, targeting decisions are often based on structural interpretations of regional gravity and magnetic data. Rela-

tionships between the density and susceptibility distributions can potentially provide an indication of mineralization. The advantage of gravity gradiometry over other gravity methods is that the data are extremely sensitive to localized density contrasts within regional geological settings. Moreover, high quality data can be acquired over very large areas for relatively low cost from either air- or ship-borne platforms.

As a potential field, gravity gradiometry data are very challenging to interpret. While maps of the different gravity gradients or their invariants can be correlated with the existence of geological structures, such maps cannot infer the 3D density distributions of the geological structures present. 2D or 3D inversion of gravity gradiometry data to 2D or 3D density models is presented as the only practical tool for quantitative interpretation. A number of publications have discussed

\*E-mail: mzhdanov@technoimaging.com.

\*TechnoImaging, 4001 South, 700 East, Suite 500, Salt Lake City, UT 84107, USA.

3D inversion with smooth (e.g., Li 2001), and focusing (e.g., Zhdanov, Ellis and Mukherjee 2004) regularization. However, an interpretation workflow including 3D inversion can be complicated and time consuming because it is dependent on a priori models and other geological constraints.

To overcome these difficulties during the initial stages of an interpretation, a number of fast semi-automated techniques related to the Euler deconvolution methods have been developed. Fedi and Florio (2006) described five groups of methods for fast estimation of the structural index (SI) and depth to the source for a potential field: 1) classical Euler deconvolution (e.g., Thompson 1982; Stavrev 1997); 2) continuous wavelet transform (CWT) (e.g., Hornby, Boschetti and Horowitz 1999; Sathicq and Gibert 2003); 3) analytic signal (e.g., Salem and Ravat 2003; Smith and Salem 2005); 4) magnitude magnetic anomaly interpretation (Stavrev 2006); and 5) the depth-from-extreme points (DEXP) method (Fedi 2007). Most of these techniques are based on the analysis of theoretical responses from specific sources of the potential fields, such as poles, dipoles, lines of poles and lines of dipoles. These techniques estimate the source position and some parameters of the source based on the attenuation characteristics of the potential field. For example, the DEXP method (Fedi 2007) uses the extreme points of the scaled, upward-continued potential field to determine the depth to the source and the excess mass or dipole moment.

While the various Euler deconvolution methods may provide information about the sources, it is not immediately obvious how this information can be prepared as a 3D density model for improved velocity modelling or as an a priori model for 3D regularized inversion. In this paper, we present an alternative approach, one which is based on and extends the idea of potential field migration as originally introduced by Zhdanov (2002). We note that Zhdanov (2002) described the migration of gravity fields to 2D density distributions and the migration of the magnetic potential to 2D magnetization distributions. For completeness, we expand upon the works of Zhdanov (2002) and Zhdanov, Liu and Wilson (2010) to describe, in detail, the theory for 2D then 3D potential field migration for transformation of observed gravity gradiometry data into a 3D density distribution. In a subsequent paper, we will describe the extension of the migration to both 3D magnetic and magnetic gradient fields. We note that 3D potential field migration does not require any a priori information about the type of the sources, nor does it rely on regularization.

Mathematically, migration is described by an action of the adjoint operator on the observed data. This concept has long been developed for seismic wavefields (e.g., Schneider 1978;

Berkhout 1980; Claerbout 1985), and has also been developed for electromagnetic fields (Zhdanov 1988, 2002, 2009a,b), where the adjoint operators manifest themselves as the (backward) propagation of seismic or electromagnetic fields in reverse time. When applied to potential fields, migration manifests itself as a special form of downward continuation of the potential field and/or its gradients. A downward continuation is applied to the migration field, which is obtained by relocating the sources of the observed field into the upper half-space as mirror images of the true sources. Contrary to conventional downward continuation of the potential field, downward continuation of the migration field is away from the mirror images of the sources. Therefore, migration is a stable transform, similar to upward continuation. At the same time, the migration field does contain remnant information about the original source distribution, which is why it can be used for subsurface imaging. Analogous to iterative electromagnetic migration (e.g., Zhdanov 2002, 2009a,b), the adjoint operators may be applied iteratively in such a manner that iterative potential field migration is equivalent to regularized inversion.

We have previously presented 2D migration and 3D focusing inversion for marine full tensor gradiometry data acquired for salt mapping in the Nordkapp Basin, located in the Norwegian sector of the Barents Sea. We refer the readers to our previous papers (Zhdanov *et al.* 2010) for a detailed description of the marine full tensor gradiometry survey and the results. In this paper, we present a case study for the 3D migration of a 5600 line km FALCON airborne gravity gradiometry data from the historic Broken Hill mining district in Australia. We compare our results to those obtained from 3D regularized inversion, as well as to the 1:250 000 geological sheets of the area.

## 2D GRAVITY AND GRAVITY GRADIENT FIELDS AND THEIR ADJOINT OPERATORS

For completeness, we begin our exposition with the case of 2D gravity fields (Zhdanov 2002) and 2D gravity gradient fields. The gravity field  $\mathbf{g} = (g_x, g_z)$  of a 2D distribution of masses concentrated with a density  $\rho(x, z)$  can be described by a complex intensity:

$$g(\zeta) = -g_x(x, z) + ig_z(x, z), \quad (1)$$

where  $\zeta = x + iz$  is a complex coordinate of the point  $(x, z)$  in the vertical plane XZ. The function  $g(\zeta)$  satisfies the following

equation (Zhdanov 2002):

$$\frac{\partial}{\partial \zeta^*} g(\zeta) = 2\pi\gamma\rho, \quad (2)$$

where  $\gamma$  is the universal constant of gravitation.

The solution of equation (2) is governed by the following expression:

$$g(\zeta') = A^g(\rho) = -2\gamma \iint_{\Gamma} \frac{1}{\zeta - \zeta'} \rho(\zeta) ds, \quad (3)$$

where  $\rho(\zeta) = \rho(x, z)$  and  $A^g(\rho)$  denotes the forward operator for a gravity field (Zhdanov 1988).

The gravity field can be expressed as the first spatial derivative of the gravity potential,  $U(x, z)$ . The second spatial derivatives of the gravity potential,  $U(x, z)$ ,

$$g_{\alpha\beta}(\mathbf{r}) = \frac{\partial^2}{\partial\alpha\partial\beta} U(\mathbf{r}), \quad \alpha, \beta = x, z, \quad (4)$$

form a symmetric gravity tensor:

$$\hat{\mathbf{g}} = \begin{bmatrix} g_{xx} & g_{xz} \\ g_{zx} & g_{zz} \end{bmatrix}, \quad (5)$$

where:

$$g_{\alpha\beta} = \frac{\partial g_{\alpha}}{\partial\beta}, \quad \alpha, \beta = x, z. \quad (6)$$

The terminologies of the gravity tensor and gravity gradiometry or gradient(s) are synonymous in the literature and in the following we will preferentially use the terms gravity gradiometry or gradient(s).

Let us define a complex intensity of the gravity gradient field,  $g_T(\zeta)$ , as a complex derivative of the complex intensity of the gravity field  $g(\zeta)$ , introduced by equation (1):

$$g_T(\zeta) = \frac{\partial g(\zeta)}{\partial\zeta} = \frac{1}{2} \left( \frac{\partial}{\partial x} - i \frac{\partial}{\partial z} \right) g(\zeta). \quad (7)$$

Substituting equation (1) into equation (7), we obtain:

$$g_T(\zeta) = g_{zz}(x, z) + i g_{zx}(x, z). \quad (8)$$

Equation (8) takes into account the symmetry of the gravity gradients, i.e.,  $g_{zx} = g_{xz}$  and the fact that the gravity potential outside the source(s) must satisfy the Laplace equation:

$$g_{xx}(x, z) + g_{zz}(x, z) = 0. \quad (9)$$

According to equations (3) and (7), we have the following expression for the complex intensity of the gravity gradient field:

$$g_T(\zeta') = A_T(\rho) = -2\gamma \iint_{\Gamma} \frac{1}{(\zeta - \zeta')^2} \rho(\zeta) ds, \quad \zeta' \notin \Gamma, \quad (10)$$

where  $A_T(\rho)$  denotes the corresponding forward operator. Note that both the gravity field  $g(\zeta')$  and the gravity gradients  $g_T(\zeta')$  are described by analytical functions outside the sources,  $\zeta' \notin \Gamma$  (Zhdanov 1988). The analytical representations derived above for the gravity and gravity gradient fields provide a useful tool for the solution of inversion and migration problems.

Mathematically, migration is the action of the adjoint operator upon the observed data. The closed form of the adjoint operator for a complex 2D gravity field was first developed by Zhdanov (2002). The adjoint gravity operator,  $A^{g*}$ , applied to some function,  $f(\zeta')$ , is given by the following:

$$A^{g*}(f) = 2\gamma \int_{-\infty}^{\infty} \frac{f^*(x')}{x' - \zeta} dx'. \quad (11)$$

Using a derivation similar to the one discussed in Zhdanov (2002) for the adjoint gravity operator, one can find that the adjoint gravity gradient operator,  $A_T^*$ , applied to some function  $f(\zeta')$ , is given by the following:

$$A_T^*(f) = -2\gamma \int_L \frac{f^*(\zeta')}{(\zeta - \zeta')^2} d\zeta'. \quad (12)$$

We examine the physical significance of the adjoint gravity gradient operator in Appendix A.

## MIGRATION OF 2D GRAVITY AND GRAVITY GRADIOMETRY FIELDS

Zhdanov (2002) introduced the *migration gravity field*,  $g_{\Gamma}^m(\zeta)$ , as a result of the application of the adjoint gravity operator,  $A^{g*}$ , to the complex intensity,  $g(\zeta)$ , of the observed gravity field, multiplied by a coefficient,  $(i/4\pi\gamma)$ :

$$g_{\Gamma}^m(\zeta) = \frac{i}{4\pi\gamma} A^{g*} g_{\Gamma}. \quad (13)$$

It was also shown that if the line of observations,  $L$ , coincides with the horizontal axis,  $z = 0$ , the migration is equivalent to downward continuation of the complex conjugate of the observed field. Downward continuation of the observed gravity and migration fields are significantly different. The gravity field has singular points in the lower half-plane associated with sources, so its analytic continuation can only be extended down to these singularities. This makes it an ill-posed and unstable transform (e.g., Strakhov 1970a,b; Zhdanov 1988). On the contrary, migration fields are analytical everywhere in the lower half-plane, meaning that migration is a well posed and stable transform.

It is demonstrated in Appendix A that the adjoint gravity gradient operator is equal to the differentiation of the

downward continued complex conjugate of the observed gravity gradient field. We call this transformation a *gravity gradient field migration* and will use the following notation:

$$g_T^m(\zeta) = \frac{\partial}{\partial \zeta} g_{T^*}(\zeta) = \frac{i}{4\pi\gamma} A_T^* g_T. \quad (14)$$

Migration of the complex intensities of the gravity and gravity gradiometry fields are largely similar. Both of these transformations are based on the downward continuation of the respective adjoint fields. The main difference is that an additional differential operation is required for the migration of the complex intensity of the gravity gradient fields, whereas only downward continuation is required for the migration of the complex intensity of the gravity field.

Migration sheds new light on the basic principles of the Depth from EXtreme Points (DEXP) method (Fedi 2007). The DEXP method uses the extreme points of the scaled, upward-continued potential field to determine the depth of the source(s). It is demonstrated in Appendix A that the sources of the migration field are the mirror images of the true sources of the potential field with respect to the real axis,  $x$  (see Figure 1). This is why the extreme points defined by the DEXP method correspond to the sources of the migration field, which reflects the true source position as a mirror image of the sources.

We should note, however, that applying the adjoint operator directly to the observed gravity and/or gravity gradient fields does not produce adequate images of the subsurface density distributions. An appropriate spatial weighting operator must be applied to the migration field in order to image

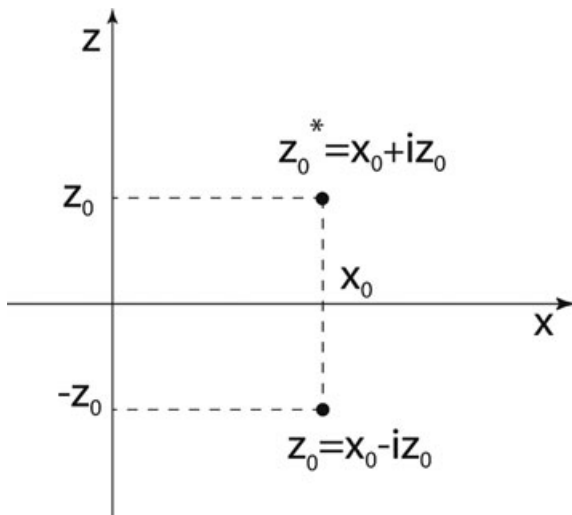


**Figure 1** The source of the observed field is a material point located at the depth  $-z_0$ , while the source of the migration field is a material point located at the height  $+z_0$  (from Zhdanov 2002).

the sources at their correct locations. This weighting operator is calculated from the integrated sensitivities of the gravity gradient data with respect to density.

It was demonstrated by Zhdanov (2002) that, using gravity migration, one can find the first approximation for the distribution of the density of the gravity field sources, described by the following expression:

$$\rho_1^g(\zeta) = k_g w_g^{-2}(z) \operatorname{Re} A^{g*} g_\Gamma = -4\pi\gamma k_g w_g^{-2}(z) \operatorname{Re} [i g_\Gamma^m(\zeta)], \quad (15)$$

where:

$$k_g = \frac{\|A^{g w*} g_\Gamma\|_M^2}{\|A^{g w} A^{g w*} g_\Gamma\|_D^2}, \quad (16)$$

$$A^{g w} = A^g W_g^{-1}. \quad (17)$$

The linear weighting operator,  $W_g$ , is the linear operator multiplying the density,  $\rho$ , by a function,  $w_g$ , equal to the square root of the integrated sensitivity of the complex intensity of the gravity field,  $S_g$ :

$$w_g = \sqrt{S_g}, \quad (18)$$

where  $S_g$  can be evaluated from the following:

$$S_g = 2\gamma \sqrt{\frac{\pi}{|z|}}, \quad z < 0. \quad (19)$$

Equation (15) is called a *gravity migration density*,  $\rho_m^g(\zeta)$ :

$$\rho_m^g(\zeta) = -4\pi\gamma k_g w_g^{-2}(z) \operatorname{Re} [i g_\Gamma^m(\zeta)], \quad (20)$$

which is proportional to the weighted real part of the gravity migration field,  $g_\Gamma^m$ . Thus, migration transformation with spatial weighting provides a stable algorithm for calculating the gravity migration density. We note that the weighting operator,  $W_g$ , plays the same role as the scaling function of the DEXP method. The important difference is that, in the case of migration, our approach to the definition of the scaling operator is based on the integrated sensitivity.

In a similar way, we can introduce a *gravity gradient migration density*,  $\rho_m^T(\zeta)$ :

$$\rho_m^T(\zeta) = k_T w_T^{-2}(z) \operatorname{Re} A_T^{w*} g_T, \quad (21)$$

where:

$$k_T = \frac{\|A_T^{w*} g_T\|_M^2}{\|A_T^w A_T^{w*} g_T\|_D^2}, \quad (22)$$

and where the function  $w_T$  is equal to the square root of the integrated sensitivity of the complex intensity of the gravity gradients,  $S_T$ :

$$w_T = \sqrt{S_T}. \quad (23)$$

The integrated sensitivity of the gravity gradient field is calculated by equation (B6) of Appendix B. Substituting this equation into equation (23), we have:

$$w_T = \sqrt{\gamma \sqrt{\frac{2\pi}{|z|^3}}}, \quad z < 0. \tag{24}$$

Equation (21) for a gravity gradient migration density can be written as follows:

$$\rho_m^T(\zeta) = k_T w_T^{-2}(z) \operatorname{Re} A_T^{w*} g_T = -4\pi \gamma k_T w_T^{-2}(z) \operatorname{Re} [i g_T^m(\zeta)]. \tag{25}$$

It is proportional to the magnitude of the weighted gradient migration field,  $g_T^m$ . Migration is a stable algorithm for calculating the migration density. Substituting equation (24) for the weighting function,  $w_T$ , back into equation (25), we find:

$$\begin{aligned} \rho_m^T(\zeta) &= -4\pi \gamma k_T \left( \gamma \sqrt{\frac{2\pi}{|z|^3}} \right)^{-1} \operatorname{Re} [i g_T^m(\zeta)] \\ &= -2\sqrt{2\pi |z|^3} k_T \operatorname{Re} [i g_T^m(\zeta)]. \end{aligned} \tag{26}$$

Let us examine the basic properties of the migration density distribution  $\rho_m^T(\zeta)$ . Using representation (14) of the migration field generated by sources shifted to the upper half-plane (see Appendix A) and taking into account equation (65), we compute the real part of  $i g_T^m$ :

$$\begin{aligned} \operatorname{Re} [i g_T^m] &= -2\gamma \operatorname{Re} \left[ i \frac{\partial}{\partial \zeta} \iint_{\Gamma^*} \frac{1}{(\tilde{\zeta} - \zeta)^2} \tilde{\rho}(\tilde{\zeta}) d\tilde{s} \right] \\ &= 4\gamma \iint_{\Gamma^*} \frac{3(\tilde{x}-x)^2(\tilde{z}-z) - (\tilde{z}-z)^3}{[(\tilde{x}-x)^2 + (\tilde{z}-z)^2]^3} \tilde{\rho}(\tilde{\zeta}) d\tilde{s}, \quad z < 0. \end{aligned} \tag{27}$$

Substituting equation (27) into equation (26), we obtain:

$$\begin{aligned} \rho_m^T(\zeta) &= -2\sqrt{2\pi |z|^3} k_T \operatorname{Re} [i g_T^m(\zeta)] \\ &= -8\gamma k_T \sqrt{2\pi |z|^3} \iint_{\Gamma^*} \frac{3(\tilde{x}-x)^2(\tilde{z}-z) - (\tilde{z}-z)^3}{[(\tilde{x}-x)^2 + (\tilde{z}-z)^2]^3} \tilde{\rho}(\tilde{\zeta}) d\tilde{s}. \end{aligned} \tag{28}$$

For example, if the real density distribution is given by a delta function,  $\rho(\zeta) = \rho_0 \delta(\zeta - \zeta_0)$ ,  $\zeta_0 = x_0 - iz_0 \in \Gamma$ , then the density  $\tilde{\rho}(\tilde{\zeta}) = \rho_0 \delta(\tilde{\zeta} - \zeta_0^*)$ , and  $\zeta_0^* = x_0 + iz_0 \in \Gamma^*$ . This means that the source of the observed field is a material point located at a depth of  $-z_0$ , while the source of the migration field is a material point located at a height of  $+z_0$  (Fig. 1). In this case we have:

$$\iint_{\Gamma^*} \frac{3(\tilde{x}-x)^2(\tilde{z}-z) - (\tilde{z}-z)^3}{[(\tilde{x}-x)^2 + (\tilde{z}-z)^2]^3} \tilde{\rho}(\tilde{\zeta}) d\tilde{s}$$

$$= \frac{3(\tilde{x}-x)^2(\tilde{z}-z) - (\tilde{z}-z)^3}{[(x_0-x)^2 + (z_0-z)^2]^3} \rho_0. \tag{29}$$

Substituting equation (29) into equation (28), we find:

$$\begin{aligned} \rho_m^T(x, z) \\ = -8\gamma k_T \sqrt{2\pi |z|^3} \frac{3(x_0-x)^2(z_0-z) - (z_0-z)^3}{[(x_0-x)^2 + (z_0-z)^2]^3} \rho_0, \quad z < 0. \end{aligned} \tag{30}$$

Differentiation of the function  $\rho_m^T(x, z)$  shows an extremum at the location of the point source  $(x_0, z_0)$ . The proof of this statement is left to the reader.

Figure 2 presents images of the gravity migration and gravity gradient migration density distributions. For both cases, one can see that the distributions have a local maximum at

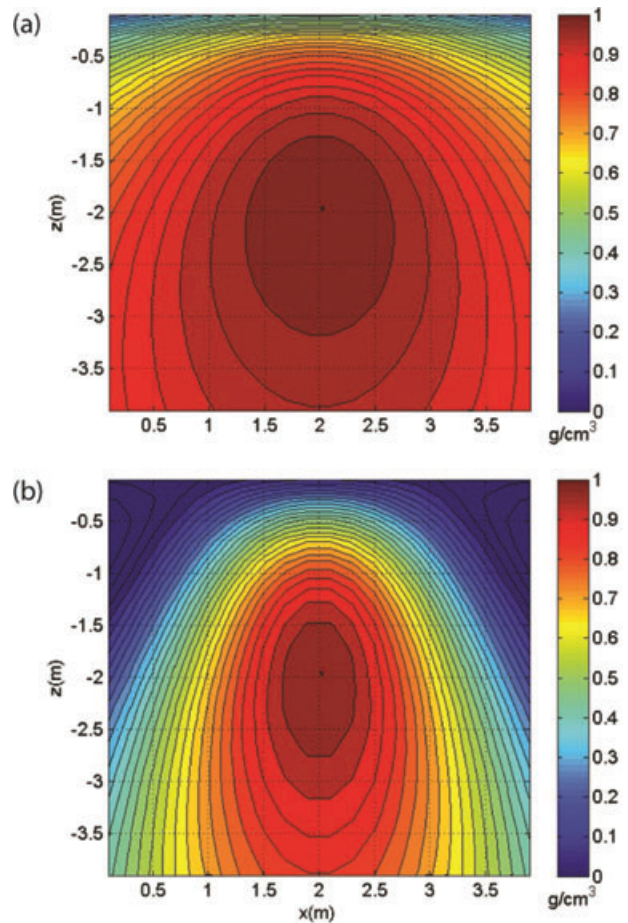
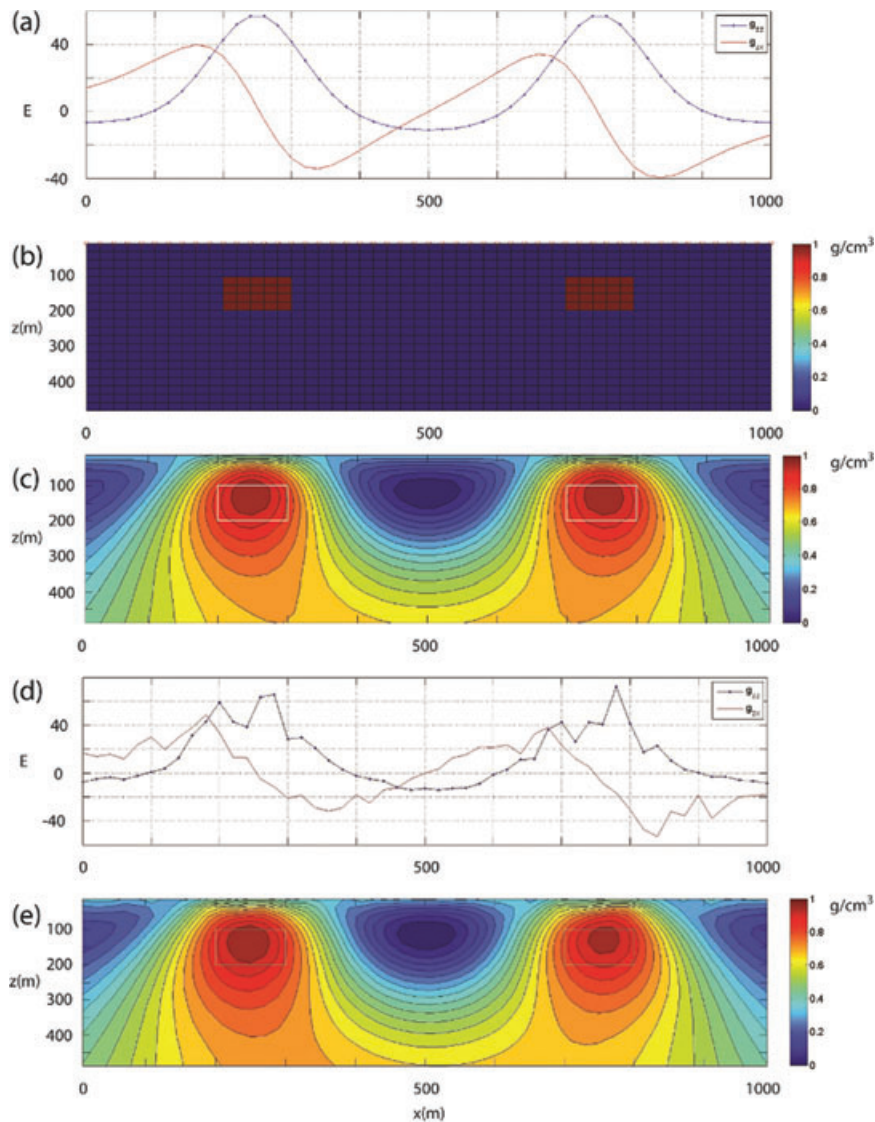


Figure 2 Following Zhdanov (2002), maps are shown of a) the gravity migration density and b) the gravity gradiometry migration density. The actual density function has a local maximum at the position of the point source (2,-2).



**Figure 3**  $g_{zx}$  and  $g_{xx}$  data with no noise. b) A vertical cross-section of the true model beneath a profile of two parallelepipeds with a  $1 \text{ g/cm}^3$  density contrast. c) A gravity gradient migration density image for  $g_{zx}$  and  $g_{xx}$  data with no noise. (d)  $g_{zx}$  and  $g_{xx}$  data with 50% random Gaussian noise. (e) A gravity gradient migration density image for  $g_{zx}$  and  $g_{xx}$  data with 50% random Gaussian noise.

the position of the point source  $(x_0, z_0)$ . However, one can see that the migration of the gradient fields produces a much more focused image than the migration of the gravity field itself.

#### MODEL STUDY: 2D MIGRATION OF GRAVITY GRADIOMETRY DATA

In this section, we consider several synthetic examples of gravity gradiometry migration. First, we consider a model formed by two rectangular parallelepipeds with a density of  $1 \text{ g/cm}^3$ ,

located at the same depth of 100 m below the observation profile (Fig. 3b). The profile of observations coincides with the  $x$  axis of the Cartesian coordinates and is perpendicular to the strike of the parallelepipeds. The long side of each parallelepiped has a strike length of 1 km along the  $y$  axis, while the vertical cross-section has an area of  $100 \text{ m} \times 100 \text{ m}$ . This model can be approximated by a 2D field and a complex intensity of the gravity gradients,  $g_T(\zeta)$ , is provided by the following expression:

$$g_T(\zeta) = g_{zz}(x, z) + i g_{zx}(x, z). \quad (31)$$

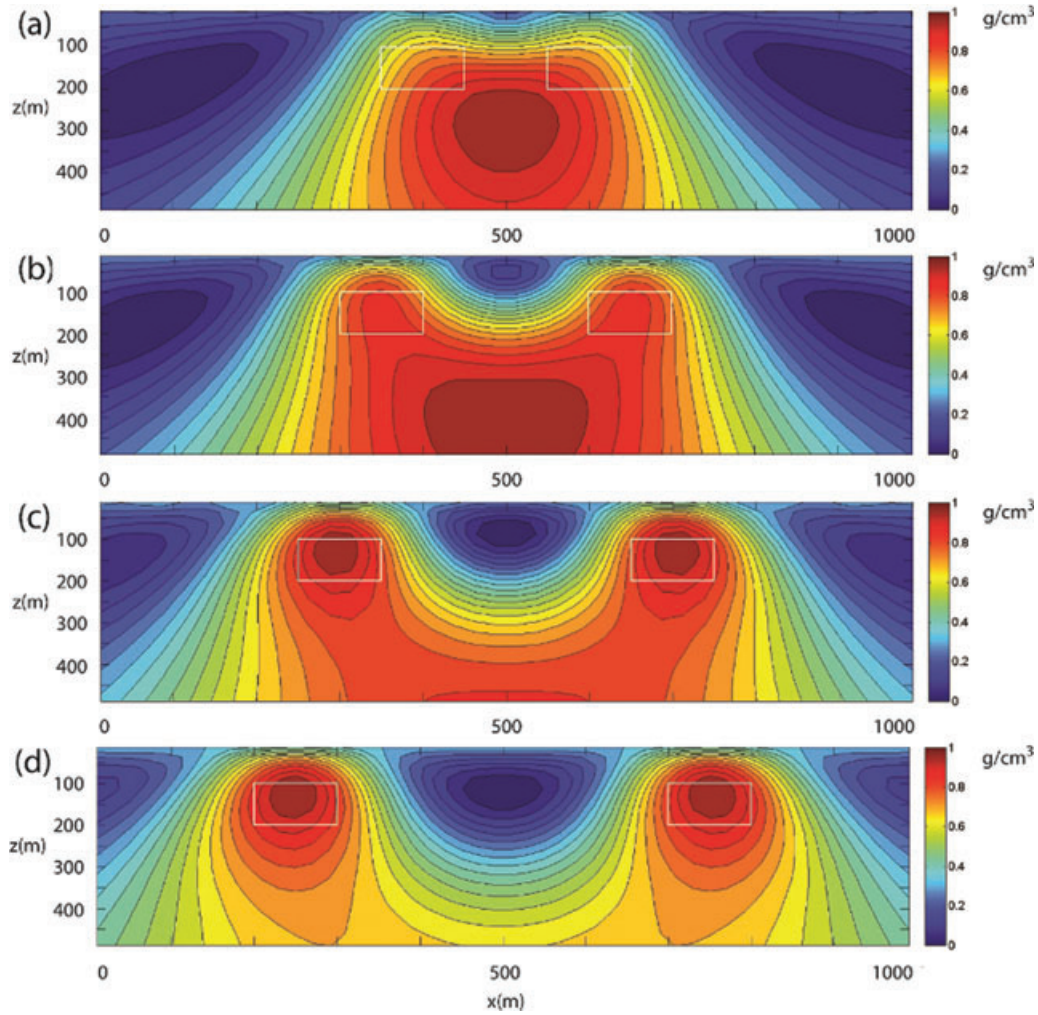


**Figure 4** Gravity gradient migration density images for  $g_{zx}$  and  $g_{xx}$  data with no noise for two parallelepipeds with a  $1 \text{ g/cm}^3$  density contrast separated by a) 100 m, b) 200 m, c) 300 m and d) 400 m.

We begin our study with a case where the separation between the two parallelepipeds along the  $x$  axis is equal to 400 m. Figure 3(a) shows plots of the gravity gradient components  $g_{zz}(x, 0)$  and  $g_{zx}(x, 0)$  along the profile of observation. We have assumed that the data were observed at 21 points with the distance,  $\Delta x$ , between the observation points equal to 20 m. These gravity gradiometry data were numerically migrated into the lower half-plane using a discrete form of the gravity gradient migration operator (14):

$$\begin{aligned}
 g_T^m(\zeta) &= \frac{i}{4\pi\gamma} A^{g^*} g_T \approx -\frac{i}{2\pi} \sum_{n=-N}^N \frac{g_T^*(n\Delta x)}{(\zeta - n\Delta x)^2} \Delta x \\
 &= \frac{\Delta x}{2\pi} \sum_{n=-N}^N \frac{g_{zx}(x, z) - i g_{zz}(x, z)}{(\zeta - n\Delta x)^2}, \quad \text{where } \zeta = x + iz.
 \end{aligned}
 \tag{32}$$

The gravity gradient migration density,  $\rho_m^T(\zeta)$ , was calculated from the gravity gradient migration field,  $g_T^m(\zeta)$ , according to equation (26). Figure 3(c) shows a map of the gravity gradient migration density,  $\rho_m^T(\zeta)$  in the vertical plane ( $x, z$ ). The correct locations of the two bodies can be clearly recovered. In order to check the sensitivity of the potential field migration against noise in the data, we have contaminated the observed data by 50% random Gaussian noise, as shown in Fig. 3(d). Figure 3(e) shows the results of the migration of noisy data. Surprisingly, migration produces a very robust image of the density distribution.

Next, we investigated the spatial resolution of migration imaging. Figure 4 shows the results of gravity gradient migration for two bodies located at different separations: 100 m, 200 m, 300 m and 400 m. Up to the point where the

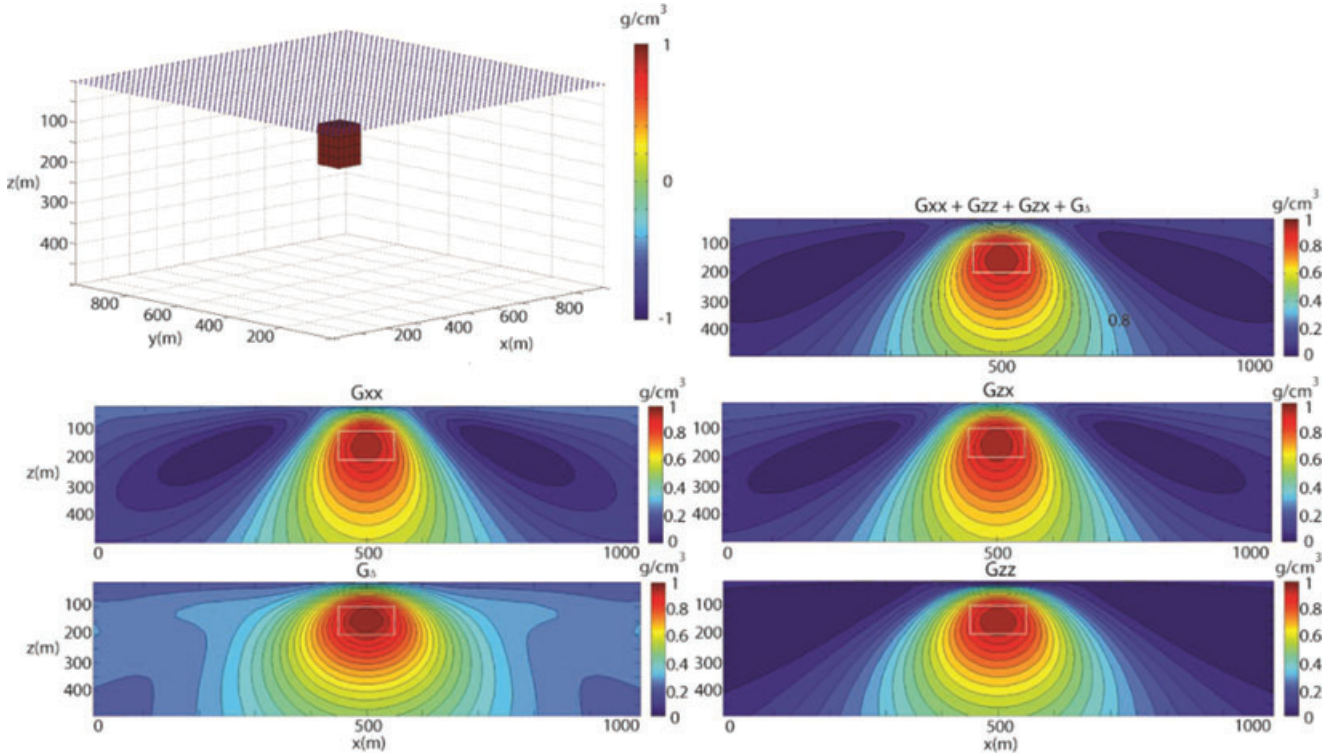


**Figure 5** 3D migration for a cube with a density of  $1 \text{ g/cm}^3$  located at a depth of 100 m below the observation surface (top right). Vertical cross-sections of the density models through the centre of the body as recovered from 3D migration of different gravity gradients ( $g_{xx}$ ,  $g_{zx}$ ,  $g_{\Delta}$  and  $g_{zz}$ ) as well as joint migration of all gravity gradients ( $g_{xx}$ ,  $g_{zx}$ ,  $g_{\Delta}$  and  $g_{zz}$ ). In all cross-sections, the body's actual outline is shown in white.

distance between the bodies is equal to their depth, migration can resolve the discrete bodies. This is an inherent limitation of the gravity method due to equivalent sources and not our migration imaging.

### 3D GRAVITY AND GRAVITY GRADIENT FIELDS AND THEIR ADJOINT OPERATORS

Following our discussion on 2D gravity and gravity gradient fields, we now consider the general case of transforming 3D gravity and gravity gradiometry data to a 3D density distribution. In a general 3D case the gravity field is given by the following equation:

$$\mathbf{g}(\mathbf{r}) = \gamma \iiint_D \rho(\mathbf{r}') \frac{\mathbf{r}' - \mathbf{r}}{|\mathbf{r}' - \mathbf{r}|^3} d\mathbf{v}', \quad (33)$$

where integration is conducted over the variable  $\mathbf{r}'$ . The second spatial derivatives of the gravity potential form a symmetric *gravity tensor*:

$$\hat{\mathbf{g}} = \begin{bmatrix} g_{xx} & g_{xy} & g_{xz} \\ g_{yx} & g_{yy} & g_{yz} \\ g_{zx} & g_{zy} & g_{zz} \end{bmatrix},$$

where:

$$g_{\alpha\beta} = \frac{\partial g_{\alpha}}{\partial \beta}, \quad \alpha, \beta = x, y, z. \quad (34)$$

According to equation (33), we have the following expression for the gravity field components:

$$g_{\alpha}(\mathbf{r}) = A_{\alpha}^g(\rho) = \gamma \iiint_D \frac{\rho(\mathbf{r}')}{|\mathbf{r}' - \mathbf{r}|^3} K_{\alpha}(\mathbf{r}' - \mathbf{r}) d\mathbf{v}', \quad \mathbf{r} \notin D, \quad (35)$$

where  $A_{\alpha}^g(\rho)$ ,  $\alpha = x, y, z$ , denotes the forward modelling operator for different gravity field components and the kernel  $K_{\alpha}(\mathbf{r}' - \mathbf{r})$  is equal to:

$$K_{\alpha}(\mathbf{r}' - \mathbf{r}) = \alpha' - \alpha, \quad \alpha = x, y, z. \quad (36)$$

The expressions for the gravity tensor components can be calculated based on equations (34) and (35):

$$g_{\alpha\beta}(\mathbf{r}) = A_{\alpha\beta}^g(\rho) = \gamma \iiint_D \frac{\rho(\mathbf{r}')}{|\mathbf{r}' - \mathbf{r}|^3} K_{\alpha\beta}(\mathbf{r}' - \mathbf{r}) d\mathbf{v}', \quad (37)$$

where  $A_{\alpha\beta}^g(\rho)$ ,  $\alpha, \beta = x, y, z$ , denotes the forward modelling operator for different gravity tensor field components and the



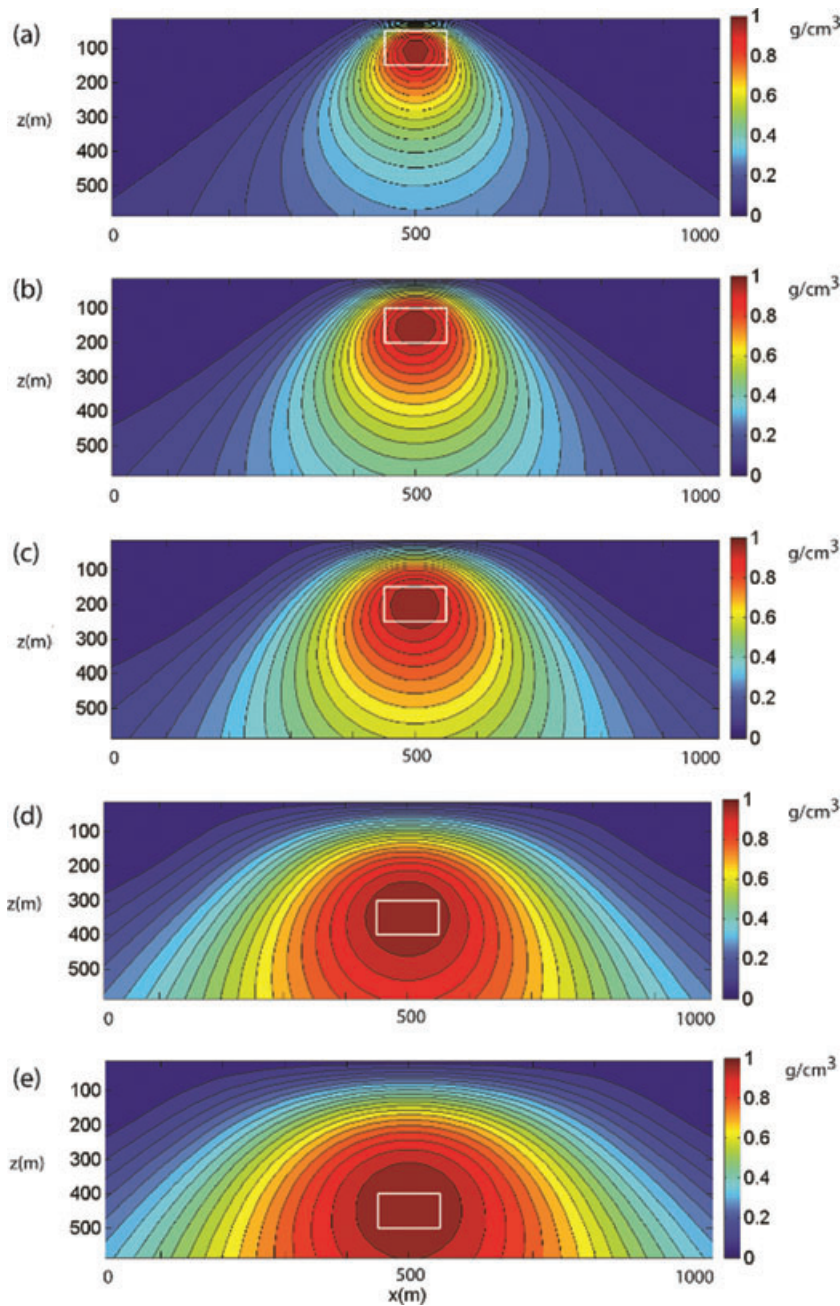


Figure 6 Vertical cross-sections of gravity gradient migration density from 3D migration of a  $g_{zz}$  and  $g_{\Delta}$  data with no noise above a single body with a  $1 \text{ g/cm}^3$  density contrast buried at a) 50 m depth, b) 100 m depth, c) 150 m depth, d) 300 m depth and e) 400 m depth.

kernels,  $K_{\alpha\beta}$ , are equal to the following:

$$K_{\alpha\beta}(\mathbf{r}' - \mathbf{r}) = \begin{cases} 3 \frac{(\alpha - \alpha')(\beta - \beta')}{|\mathbf{r}' - \mathbf{r}|^2}, & \alpha \neq \beta \\ 3 \frac{(\alpha - \alpha')^2}{|\mathbf{r}' - \mathbf{r}|^2} - 1, & \alpha = \beta \end{cases}, \quad \alpha, \beta = x, y, z. \quad (38)$$

In addition to the gravity tensor components described by equations (37) and (38), the gravity gradiometers also measure

the difference between the gradients:

$$g_{\Delta} = \frac{1}{2}(g_{xx} - g_{yy}), \quad (39)$$

which can be expressed as

$$g_{\Delta} = \gamma \iiint_D \frac{\rho(\mathbf{r}')}{|\mathbf{r}' - \mathbf{r}|^3} K_{\Delta}(\mathbf{r}' - \mathbf{r}) dv', \quad (40)$$

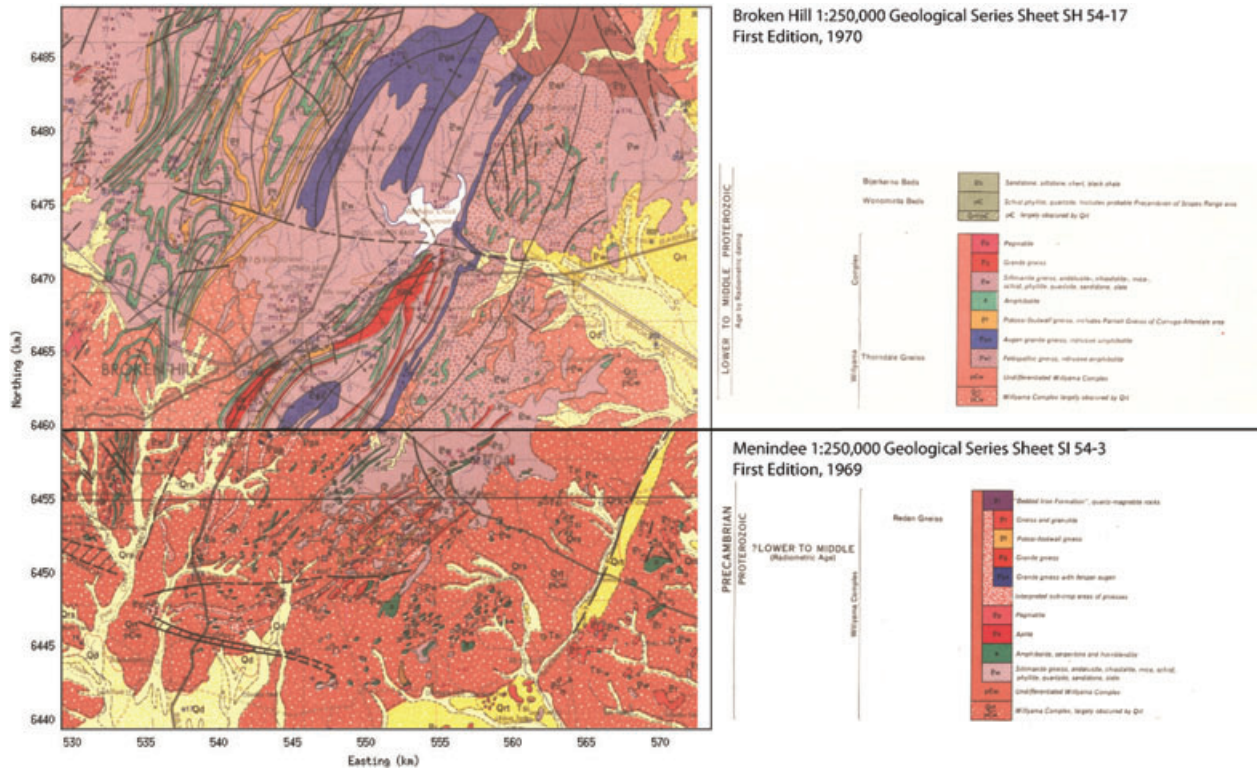
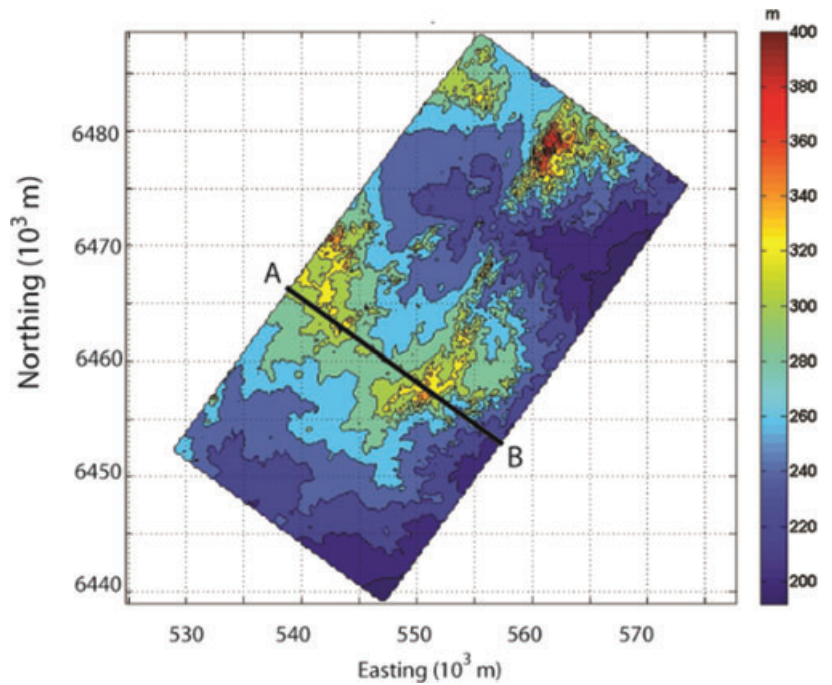


Figure 7 Geology of the Broken Hill area, prepared from the Broken Hill and Menindee 1:250 000 geological maps (available from Geoscience Australia).

Figure 8 Topography of the Broken Hill FALCON survey area. Profile A–B extends across the Broken Hill deposit and will be referred to in subsequent figures.



where

$$K_{\Delta}(\mathbf{r}' - \mathbf{r}) = \frac{3}{2} \frac{(x' - x)^2 - (y' - y)^2}{|\mathbf{r}' - \mathbf{r}|^3}. \quad (41)$$

Using the technique described in Zhdanov (2002), it can be demonstrated that the adjoint operator  $A^{\alpha*}$  for the gravity problem is equal to:

$$A_{\alpha}^*(f) = \gamma \iint_S \frac{f(\mathbf{r})}{|\mathbf{r}' - \mathbf{r}|^3} K_{\alpha}(\mathbf{r}' - \mathbf{r}) ds. \quad (42)$$

The adjoint operator for gravity gradients is given by the following equations:

$$A_{\alpha\beta}^*(f) = \iint_S \frac{f(\mathbf{r})}{|\mathbf{r}' - \mathbf{r}|^3} K_{\alpha\beta}(\mathbf{r}' - \mathbf{r}) ds, \quad (43)$$

$$A_{\Delta}^*(f) = \iint_S \frac{f(\mathbf{r})}{|\mathbf{r}' - \mathbf{r}|^3} K_{\Delta}(\mathbf{r}' - \mathbf{r}) ds. \quad (44)$$

We will use equations (42)–(44) for introducing the 3D gravity and gravity gradiometry migration fields.

### MIGRATION OF 3D GRAVITY AND GRAVITY GRADIOMETRY FIELDS

As in the 2D case, the *migration gravity field*,  $g_{\alpha}^m(\mathbf{r})$ , is introduced as a result of the application of the adjoint gravity operator,  $A_{\alpha}^*$ , to the observed component of the gravity field:

$$g_{\alpha}^m(\mathbf{r}) = A_{\alpha}^* g_{\alpha}, \quad (45)$$

where the adjoint operator  $A^{\alpha*}$  for the gravity problem is given by equation (42). From a physical point of view, the migration field is obtained by moving the sources of the observed gravity field above the observational surface. Nevertheless, the migration field contains some remnant information about the original sources of the gravity anomaly. This is why it can be used in imaging the sources of the gravity field.

In a similar way, we can introduce a *migration gravity tensor field*  $g_{\alpha\beta}^m(\mathbf{r})$  and use the following notations for the components of this tensor field:

$$g_{\alpha\beta}^m(\mathbf{r}) = A_{\alpha\beta}^* g_{\alpha\beta}, \quad (46)$$

$$g_{\Delta}^m(\mathbf{r}) = A_{\Delta}^* g_{\Delta}, \quad (47)$$

where the adjoint operators,  $A_{\alpha\beta}^*$  and  $A_{\Delta}^*(f)$ , applied to some function  $f(\mathbf{r})$ , are given by formulas (43) and (44). We should note, however, that the direct migration of the observed gravity and/or gravity tensor fields does not produce an adequate image of the subsurface density distribution because the migration fields rapidly attenuate with the depth, as one can see from expressions (42)–(44). In order to image the sources of

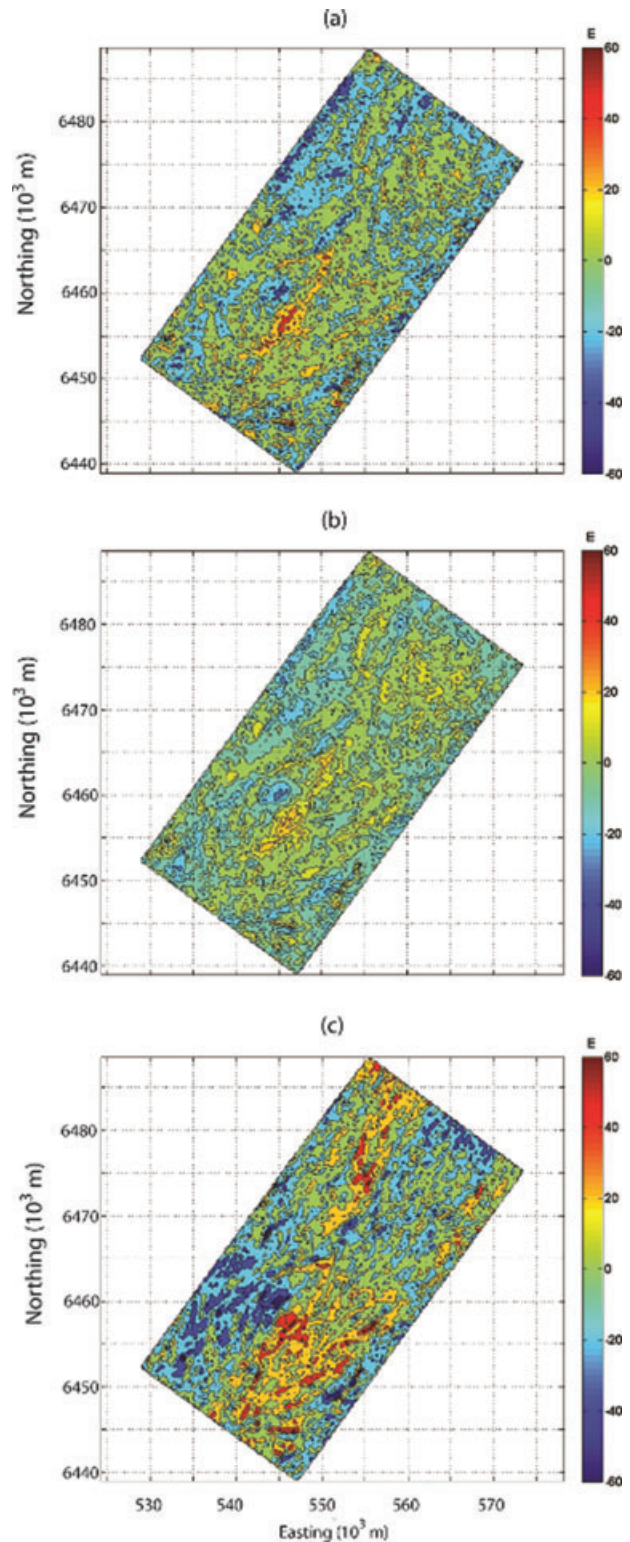


Figure 9  $g_{zz}$  data from the Broken Hill FALCON survey processed by a) Fourier domain, b) equivalent source and c) spatial convolution methods.

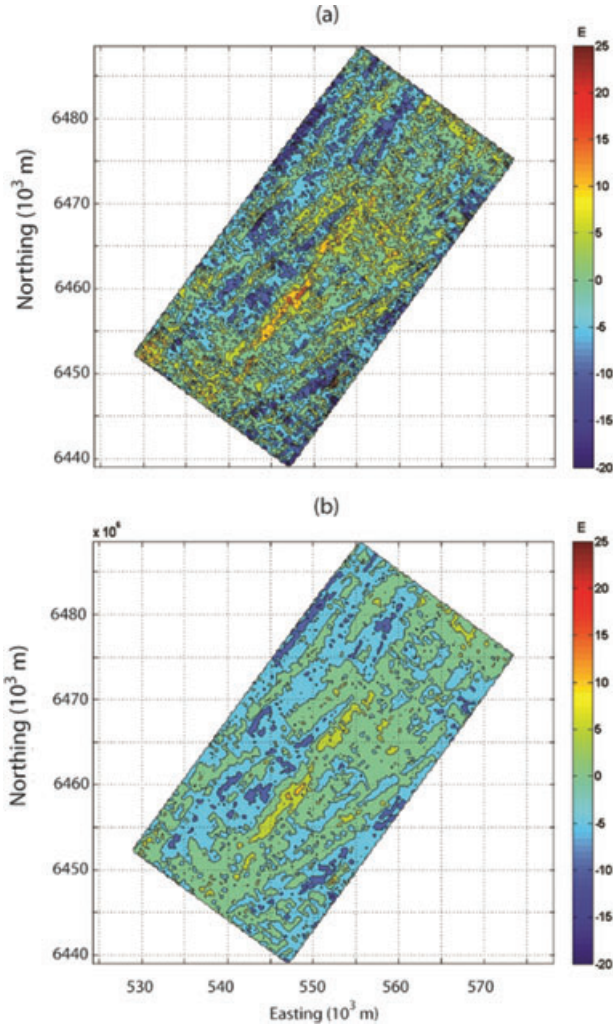


Figure 10  $g_{xy}$  data from the Broken Hill FALCON survey processed by a) Fourier-domain and b) equivalent source methods.

the gravity fields at their correct locations, one should apply an appropriate spatial weighting operator to the migration fields. This weighting operator is constructed based on the integrated sensitivity of the data to the density.

As for the 2D case (Zhdanov 2002), one can find a distribution of the density of the gravity field sources, described by the following expression:

$$\rho_{\alpha}^m(\mathbf{r}) = \lambda^{-1} (\mathbf{W}_m^* \mathbf{W}_m)^{-1} \mathbf{A}_{\alpha}^* g_{\alpha} = k_{\alpha} w_{\alpha}^{-2}(z) g_{\alpha}^m(\mathbf{r}), \quad (48)$$

where the unknown coefficient  $k_{\alpha} = \lambda^{-1}$  can be determined by a linear line search (Zhdanov 2002) and the linear weighting operator  $\mathbf{W}_m = \mathbf{W}_{\alpha}$  is selected as a linear operator of the multiplication of density  $\rho$  by a function,  $w_{\alpha}$ , equal to the square root of the integrated sensitivity of the complex intensity of

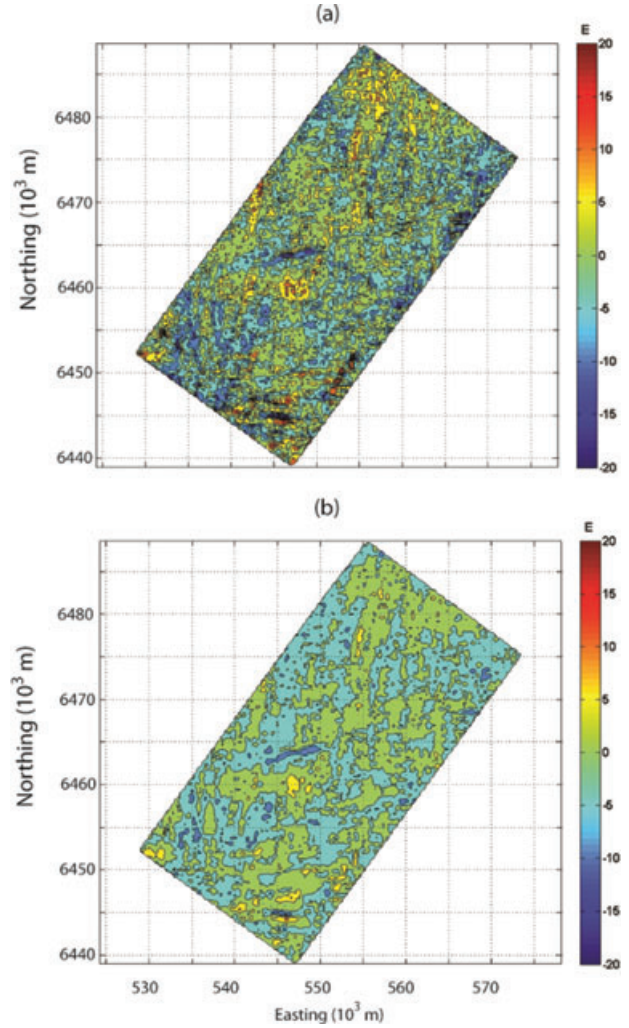


Figure 11  $g_{\Delta}$  data from the Broken Hill FALCON survey processed by a) Fourier-domain and b) equivalent source methods.

the gravity field,  $S_{\alpha}$ :

$$w_{\alpha} = \sqrt{S_{\alpha}}. \quad (49)$$

Using a technique similar to one described in Appendix B for the 2D case, one can find that  $S_{\alpha}$  is computed from the following:

$$S_{\alpha} = c_{\alpha} \frac{1}{|z|}, \quad z < 0, \quad \alpha = x, y, z, \quad (50)$$

where  $c_{\alpha}$  are the corresponding constants for different components equal to:

$$c_x = c_y = \gamma \sqrt{\frac{\pi}{2}}, \quad c_z = \gamma \sqrt{\pi}.$$

Equation (48) is called a *migration density*  $\rho_m^g(\zeta)$ :

$$\rho_\alpha^m(\mathbf{r}) = k_\alpha w_{\alpha g}^{-2}(z) g_\alpha^m(\mathbf{r}), \quad (51)$$

and it is proportional to the weighted migration field,  $g_\alpha^m$ :

$$\rho_\alpha^m(\mathbf{r}) = \frac{k_\alpha}{c_\alpha} |z| g_\alpha^m(\mathbf{r}), \quad (52)$$

where

$$g_\alpha^m(\mathbf{r}) = \iint_S \frac{g_\alpha(\mathbf{r}')}{|\mathbf{r} - \mathbf{r}'|^3} K_\alpha(\mathbf{r} - \mathbf{r}') ds'. \quad (53)$$

Thus, the migration transform with spatial weighting provides a stable algorithm for calculating the migration density.

In a similar way, we can introduce a migration density based on the gravity tensor migration:

$$\rho_{\alpha\beta}^m(\mathbf{r}) = k_{\alpha\beta} w_{\alpha\beta}^{-2}(z) g_{\alpha\beta}^m(\mathbf{r}), \quad \rho_\Delta^m(\mathbf{r}) = \gamma k_\Delta w_\Delta^{-2}(z) g_\Delta^m(\mathbf{r}), \quad (54)$$

where unknown coefficients  $k_{\alpha\beta}$  are determined by the corresponding linear line search and functions  $w_{\alpha\beta}$  and  $w_\Delta$  are equal to the square root of the integrated sensitivity of the gravity tensor fields,  $S_{\alpha\beta}$  and  $S_\Delta$ , respectively:

$$w_{\alpha\beta} = \sqrt{S_{\alpha\beta}}, \quad w_\Delta = \sqrt{S_\Delta}. \quad (55)$$

It can be demonstrated that the integrated sensitivity of the gravity tensor field is calculated from the following expressions:

$$S_{\alpha\beta} = c_{\alpha\beta} \frac{1}{z^2}, \quad S_\Delta = c_\Delta \frac{1}{z^2}, \quad (56)$$

where  $c_{\alpha\beta}$  are the corresponding constants for different tensor field components:

$$c_{zz} = c_{zx} = c_{zy} = \gamma \frac{\sqrt{3\pi}}{2}, \quad c_{xx} = c_{yy} = \gamma \frac{3\sqrt{\pi}}{4}.$$

Expression (54) is called a tensor field migration density. It is proportional to the magnitude of the weighted tensor migration field  $g_{\alpha\beta}^m$ . Substituting equation (56) for the weighting function  $w_T$  in equations (55) and (54), we find that:

$$\rho_{\alpha\beta}^m(\mathbf{r}) = \frac{k_{\alpha\beta}}{c_{\alpha\beta}} z^2 g_{\alpha\beta}^m(\mathbf{r}), \quad \rho_\Delta^m(\mathbf{r}) = \frac{k_\Delta}{c_\Delta} z^2 g_\Delta^m(\mathbf{r}), \quad (57)$$

where:

$$g_{\alpha\beta}^m(\mathbf{r}) = \iint_S \frac{g_{\alpha\beta}(\mathbf{r}')}{|\mathbf{r} - \mathbf{r}'|^3} K_{\alpha\beta}(\mathbf{r} - \mathbf{r}') ds', \quad (58)$$

$$g_\Delta^m(\mathbf{r}) = \iint_S \frac{g_\Delta(\mathbf{r}')}{|\mathbf{r} - \mathbf{r}'|^3} K_\Delta(\mathbf{r} - \mathbf{r}') ds'. \quad (59)$$

Finally, we can consider joint migration of several components of the gravity tensor. For example, we can jointly

migrate  $g_{zz}$ ,  $g_{xx}$ ,  $g_{zx}$  and the  $g_\Delta$  components and find the corresponding migration density as per the following:

$$\rho_{\alpha\beta}^m(\mathbf{r}) = z^2 \left[ \frac{k_{zz}}{c_{zz}} g_{zz}^m(\mathbf{r}) + \frac{k_{xx}}{c_{xx}} g_{xx}^m(\mathbf{r}) + \frac{k_{zx}}{c_{zx}} g_{zx}^m(\mathbf{r}) + \frac{k_\Delta}{c_\Delta} g_\Delta^m(\mathbf{r}) \right]. \quad (60)$$

Note that equation (60) can be simplified to:

$$\rho_{\alpha\beta}^m(\mathbf{r}) = z^2 [a_{zz} g_{zz}^m(\mathbf{r}) + a_{xx} g_{xx}^m(\mathbf{r}) + a_{zx} g_{zx}^m(\mathbf{r}) + a_\Delta g_\Delta^m(\mathbf{r})], \quad (61)$$

where  $a_{zz}$ ,  $a_{xx}$ ,  $a_{zx}$ , and  $a_\Delta$  can be treated as the weights of the corresponding migration fields in the density model, which can be empirically determined from model studies.

### MODEL STUDY: 3D MIGRATION OF GRAVITY GRADIOMETRY DATA

In this section we present two examples of 3D migration for gravity tensor field data. In the first example, we consider a model formed by a single cube of 100 m dimension with a density of 1 g/cm<sup>3</sup>, located at a depth of 100 m below the surface. Data for  $g_{xx}$ ,  $g_{zx}$ ,  $g_\Delta$  and  $g_{zz}$  were simulated on the horizontal plane,  $z = 0$ . First, we applied 3D migration to each of the gravity gradients and then joint 3D migration to all of the gravity gradients with equal weights. From Fig. 5, one can see that migration of each component recovered the correct location of the body. However, the images are slightly different for the different components. For example, the  $g_{zz}$  migration image has a sharper maximum in the location of the cubic body but the isolines of the migration image expand conically with the depth. The  $g_\Delta$  migration image has a slightly less sharp maximum in the location of the cubic body than the  $g_{zz}$  migration image, while the isolines of the  $g_\Delta$  migration image are more concentric around the cubic body. For joint migration, one can see that the image has a sharp maximum at the location of the cubic body as a  $g_{zz}$  image, while the isolines of the combined image are distributed relatively concentrically around the target.

Next, we considered the vertical resolution for a single cube of 100 m dimension and a density contrast of 1 g/cm<sup>3</sup>. The cube was buried with depths ranging from 50–400 m. The results of the 3D migration of  $g_{zz}$  and  $g_\Delta$  data with equal weights and no noise are shown in Fig. 6. Note that in each case, migration is able to recover a migration density that has a maximum at the centre of the actual target.

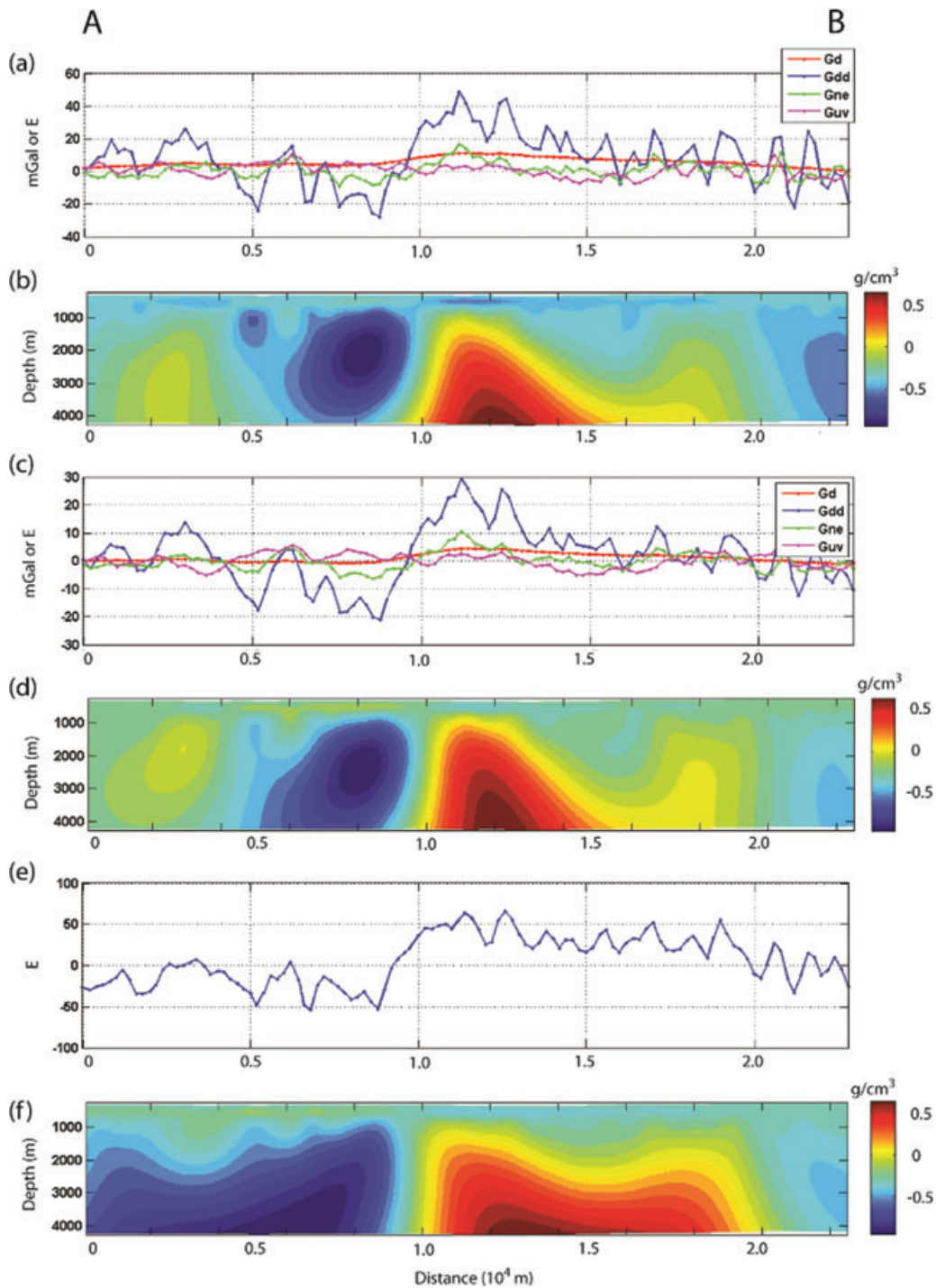


**Figure 12** a)  $g_{xy}$ ,  $g_{\Delta}$ ,  $g_{zz}$ , and  $g_z$  data processed using the Fourier-domain method across profile A–B. b) Vertical cross-section along profile A–B from 3D migration of  $g_{xy}$ ,  $g_{\Delta}$  and  $g_{zz}$  data processed using the Fourier-domain method. c)  $g_{xy}$ ,  $g_{\Delta}$ ,  $g_{zz}$  and  $g_z$  data processed using the equivalent source method across profile A–B. d) Vertical cross-section along profile A–B from 3D migration of  $g_{xy}$ ,  $g_{\Delta}$  and  $g_{zz}$  data processed using the equivalent source method. e)  $g_{zz}$  data processed using the spatial convolution method across profile A–B. f) Vertical cross-section along profile A–B from 3D migration of  $g_{zz}$  data processed using the spatial convolution method.

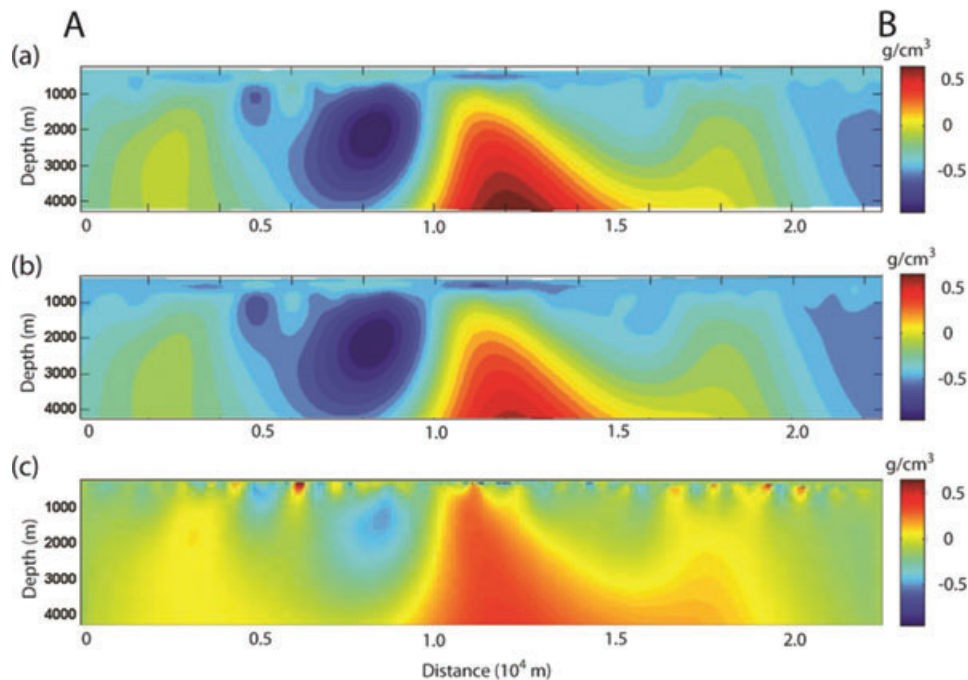


**Figure 13** Vertical cross-sections along profile A–B from a) 3D migration of  $g_{xy}$ ,  $g_{\Delta}$ ,  $g_{zz}$  data processed using the Fourier domain method, b) 3D migration of  $g_{zz}$  data processed using the Fourier domain method and c) 3D inversion of  $g_{zz}$  data processed using the Fourier domain method.

#### CASE STUDY–BROKEN HILL FALCON SURVEY

Broken Hill is a historic mining district in New South Wales (NSW), Australia and host of the world-class Broken Hill stratiform sediment-hosted Ag-Pb-Zn deposit. The host geology consists of the Willyama Supergroup of metamorphosed clastic and volcanoclastic sediments, basic to acid volcanics and intrusions of 171–1590 Ma age (Fig. 7). Mineralization is sediment exhalative in origin and subsequently modified by metamorphism, folding and shearing (e.g., Parr *et al.* 2004). Given the significant density contrast between the dense amphibolite- and garnet-altered lithologies and the metamorphosed sedimentary host rocks, gravity methods have been essential in the exploration of Broken Hill-type deposits (e.g., Isles 1979). Today, mining has virtually eliminated the gravity response of the Broken Hill ore body. Simulations have estimated the maximum  $g_{zz}$  response at 80 m ground clearance to be in the range of 10–50 Eo over the central lode, similar to the responses of amphibolite units (Lane and Peljo 2004). The following table lists rock types and their corresponding densities as detailed by Ruzskowski (1998).

The FALCON airborne gravity gradiometry (AGG) system measured the horizontal curvature components of the gravity gradient, i.e.,  $g_{xy}$  and  $g_{\Delta} = \frac{g_{xx} - g_{yy}}{2}$ . Other tensor compo-

Rock type	Density ( $\text{g}/\text{cm}^3$ )
Potosi Gneiss	2.79
Sillimanite Gneiss	2.85
Quartzite	2.65
Granite Gneiss	2.75
Amphibolite	3.20

nents were then derived from these measured components (Lee 2001). In 2003, a 5600 line km FALCON airborne gravity gradiometry survey was flown in the Broken Hill district to stimulate exploration interest for base metal, Fe-Cu-Au and Ni-Cu-Pt-Pd deposits (Lane, Milligan and Robson 2003; Lane 2006). The 44.6 km  $\times$  22.5 km survey area was flown at 200 m line spacings approximately parallel to a geological strike at 036 degrees (to ensure a maximum sampling rate), with tie lines flown every 2 km. The ground clearance was nominally 80 m flown in a drape over the topographic relief which varied from 174–421 m above sea level (Fig. 8). Hills trend approximately parallel to the flight lines. Several small pits and larger waste dumps of the Broken Hill workings are evident in the digital elevation model. All data were terrain-corrected using a density of 2.75  $\text{g}/\text{cm}^3$ . This results in a slight positive

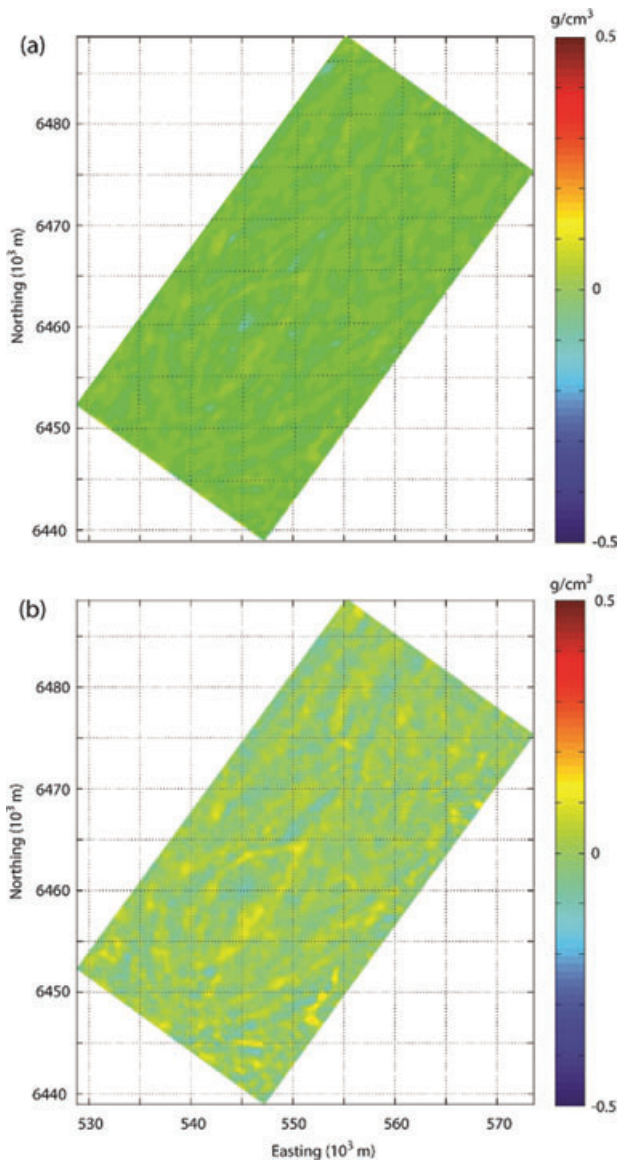


**Figure 14** Horizontal cross-sections at - 125 m above sea level ( $\sim 500$  m below the topographic peak) from a) 3D migration of  $g_{zz}$  data processed using the Fourier domain method and b) 3D inversion of  $g_{zz}$  data processed using the Fourier-domain method.

correlation between the gravity gradients and the topography, which is inferred to be acceptable on the grounds that much of the positive topographic relief is comprised of amphibolite and garnet-altered lithologies that are relatively dense compared to the metamorphosed sediment host rocks that make up the bulk of the survey area (Hensley 2003). The measured gradients were processed with three processing methods: Fourier domain, equivalent source and spatial convolution. All three processing methods treat noise differently and

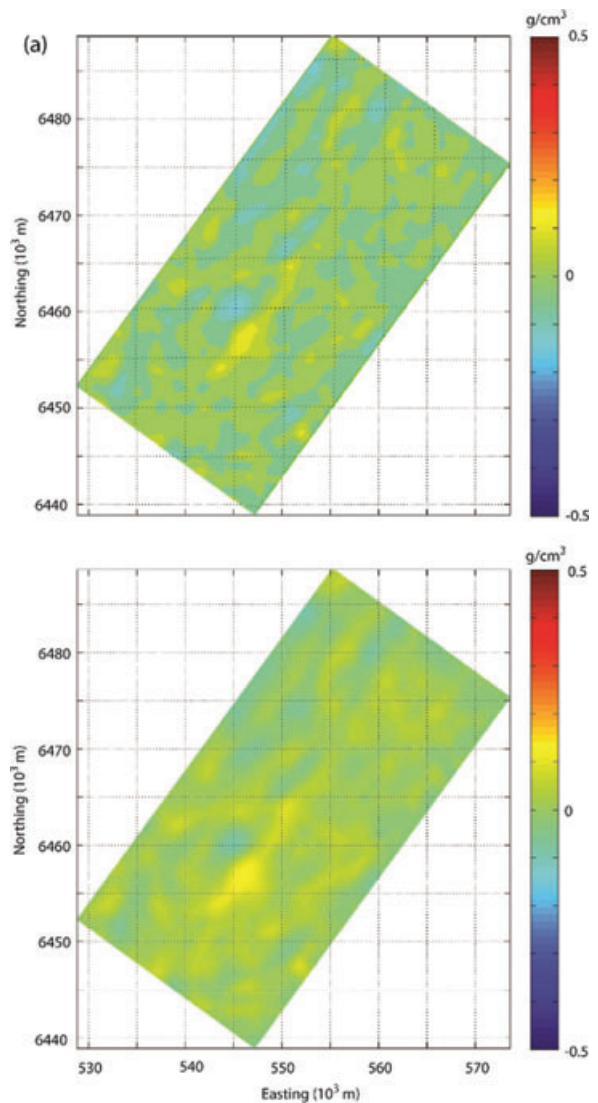


**Figure 15** Horizontal cross-sections at - 625 m above sea level ( $\sim 1000$  m below the topographic peak) from a) 3D migration of  $g_{zz}$  data processed using the Fourier-domain method and b) 3D inversion of  $g_{zz}$  data processed using the Fourier domain method.

as shown in Figs 9–11, their data range and mean variations can be quite significant.

With independent results (e.g., 3D inversion), we were able to scale the density contrasts in our 3D migration results. However, for the purpose of rapid 3D imaging, in the following we select our 3D migration images to vary between density limits of  $-0.5$  and  $+0.5$   $\text{g}/\text{cm}^3$ .

In Fig. 8, we show the location of profile A–B, which crosses the Broken Hill deposit. In Fig. 12, we show vertical cross-sections beneath profile A–B from the 3D density models



obtained from 3D migration of data processed by Fourier-domain, equivalent source and spatial convolution methods. We have also shown the data along the profile A–B. Note that there is significant variation in the amplitude of data produced from each method. This said, we note that the 3D migration model for all components of the Fourier-domain and equivalent source data show similar features, whereas there are differences from 3D migration of  $g_{zz}$  for the spatial convolution data. We were unable to perform 3D migration on any additional components of the spatial convolution data, as they were not available.

We ran our 3D migration jointly for  $g_{xy}$ ,  $g_{\Delta}$  and  $g_{zz}$ , as well as singly for  $g_{zz}$  only. For this, we considered only the data processed by the Fourier-domain method. For further comparison, we inverted  $g_{zz}$  data using 3D regularized inversion (Zhdanov *et al.* 2004). The 3D inversion had no a priori model and used smooth regularization. In Fig. 13, we show

the vertical cross-sections beneath profile A–B for the 3D density models obtained from joint 3D migration, 3D migration and 3D inversion. We note the similarity between the two 3D migration models and that they are both similar to the 3D regularized inversion results. As mentioned earlier, the amplitude of the migration results are slightly different from the inversion results because we scaled our migration results to vary between  $-0.5$  and  $+0.5$   $\text{g}/\text{cm}^3$ . For further comparison of 3D migration and 3D inversion for the  $g_{zz}$  data, Figures 14 and 15 show horizontal cross-sections at 500 m and 1000 m depth below topographic peak. Structurally, we observe very good agreement between the models. This agreement is reinforced when we overlay the regional geology, as shown in Figure 16. In particular, high density contrasts are well associated with amphibolites. Moreover, we can image subtle 3D structures, such as the Goldfinger prospect in the southern corner of the survey area.

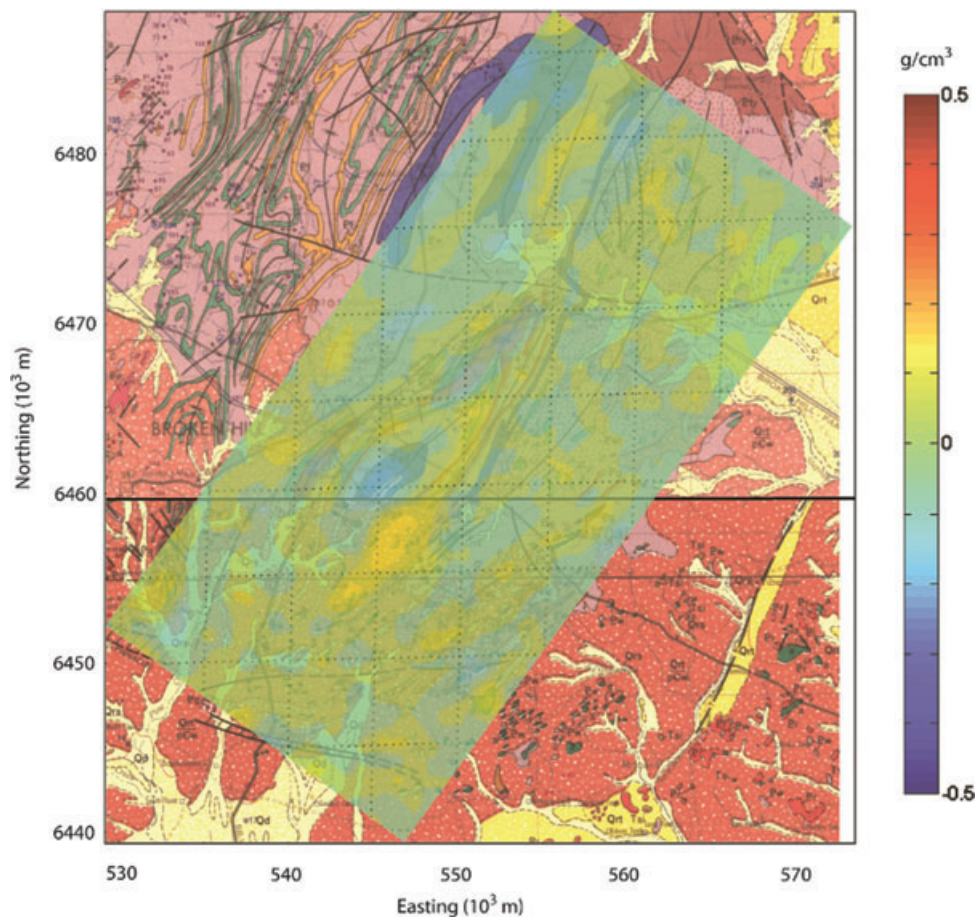


**Figure 16** Horizontal cross-section at  $\sim 625$  m above sea level ( $\sim 500$  m below the topographic peak) from 3D migration of  $g_{zz}$  data processed using the Fourier-domain method overlain with the Broken Hill area 1:250 000 geological sheets.

## CONCLUSIONS

We have introduced 2D and 3D potential field migration as a new method for rapidly imaging entire surveys of gravity and gravity gradiometry data. For gravity fields and their gradients, we have shown that potential field migration is an integral transformation of the gravity field and/or gradients into 2D or 3D density distributions. As we will show in a subsequent paper, potential field migration can also be extended to magnetic fields and/or their gradients. Potential field migration is very fast and stable and the results are fairly similar to those obtained from regularized inversion with smooth stabilizers. The migration density models can also be used as a priori models for subsequent regularized inversion with focusing stabilizers. As an analogue of iterative electromagnetic migration (e.g., Zhdanov *et al.* 2011), we note that the adjoint operators can be applied iteratively such that iterative potential field migration is comparable to regularized inversion. This is the subject of our on-going work.

We have demonstrated the practicality of imaging entire gravity gradiometry surveys with an example from a 5600 line km FALCON airborne gravity gradiometry survey over the historic Broken Hill mining district in Australia. We compared our 3D migration results with those obtained from 3D regularized inversion. We observed very good agreement between those results produced by migration and those produced by 3D regularized inversion.

## ACKNOWLEDGEMENTS

The authors acknowledge TechnoImaging for their support of this research and for permission to publish. M. Zhdanov, X. Liu and L. Wan also acknowledge the support of The University of Utah's Consortium for Electromagnetic Modeling and Inversion (CEMI) and the Center for High Performance Computing (CHPC). We are thankful to Dr Ed Biegert for his useful comments and recommendations, which helped to improve the manuscript. The Broken Hill FALCON data were released by the Geological Survey of New South Wales. We thank Dr Martin Čuma and the University of Utah's CHPC for 3D regularized inversion of the Broken Hill FALCON data.

## REFERENCES

- Berkhout A.J. 1980. *Seismic Migration*. Elsevier.  
 Claerbout J.F. 1985. *Imaging the Earth's Interior*. Blackwell Scientific Publications.  
 Fedi M. 2007. DEXP: A fast method to determine the depth

- to the sources of potential fields. *Geophysics* 72, L1–L11. doi:10.1190/1.2399452.  
 Fedi M. and Florio G. 2006. SCALFUN: 3D analysis of potential field scaling function to determine independently or simultaneously structural index and depth to source. 76<sup>th</sup> SEG meeting, New Orleans, Louisiana, USA, Expanded Abstracts. doi:10.1190/1.2372499.  
 Hensley C. 2003. *Data Processing Report (Sponsored Section), Airborne Gravity Gradiometer Survey, Broken Hill, NSW, Australia*. BHP Billiton.  
 Hornby P., Boschetti F. and Horowitz F.G. 1999. Analysis of potential field data in the wavelet domain. *Geophysical Journal International* 137, 175–196. doi:10.1046/j.1365-246x.1999.00788.x.  
 Isles D.J. 1979. A probable extension to the Willyama block in NSW. *Exploration Geophysics* 10, 191–192. doi:10.1071/EG979191.  
 Lane R. 2006. Investigations stemming from the 2003 Broken Hill airborne gravity gradiometer survey. In: *Broken Hill Exploration Initiative 2006 Conference Abstracts* (eds. R.J. Korsch and R.G. Barnes), pp. 116–128. Geoscience Australia Record 2006/21.  
 Lane R., Milligan P. and Robson D. 2003. An airborne gravity gradiometer survey of Broken Hill. In: *Broken Hill Exploration Initiative 2003 Conference Abstracts* (ed. M. Peljo), pp. 89–92. Geoscience Australia Record 2003/13.  
 Lane R. and Peljo M. 2004. Estimating the pre-mining gravity and gravity gradient response of the Broken Hill Ag-Pb-Zn deposit. *ASEG 17<sup>th</sup> Geophysical Conference and Exhibition*, Expanded Abstracts. doi:10.1071/ASEG2004ab083.  
 Lee J.B. 2001. FALCON gravity gradiometer technology. *Exploration Geophysics* 32, 247–250. doi:10.1071/EG01247.  
 Li Y. 2001. 3D inversion of gravity gradiometer data. 71<sup>st</sup> SEG meeting, San Antonio, Texas, USA, Expanded Abstracts. doi:10.1190/1.1816383.  
 Parr J.M., Stevens B.P.J., Carr G.R. and Page R.W. 2004. Subseafloor origin for Broken Hill Pb-Zn-Ag mineralization, New South Wales, Australia. *Geology* 32, 589–592. doi: 10.1130/G20358.1.  
 Ruzkowsky P. 1998. An analysis of the Broken Hill exploration initiative petrophysical database. *Exploration Geophysics* 29, 592–596. doi:10.1071/EG998592.  
 Salem A. and Ravat D. 2003. A combined analytic signal and Euler method (AN-EUL) for automatic interpretation of magnetic data. *Geophysics* 68, 1952–1961. doi:10.1190/1.1635049.  
 Sailhac P. and Gibert D. 2003. Identification of sources of potential fields with the continuous wavelet transform: Two-dimensional wavelets and multipolar approximations. *Journal of Geophysical Research* 108, 22–62. doi:10.1029/2002JB002021.  
 Schneider W.A. 1978. Integral formulation for migration in two and three dimensions. *Geophysics* 43, 49–76. doi:10.1190/1.1440828.  
 Smith R.S. and Salem A. 2005. Imaging depth, structure, and susceptibility from magnetic data: The advanced source-parameter imaging method. *Geophysics* 70, L31–L38. doi:10.1190/1.1990219.  
 Stavrev P.Y. 1997. Euler deconvolution using differential similarity transformations of gravity or magnetic anomalies. *Geophysical Prospecting* 45, 207–246. doi:10.1046/j.1365-2478.1997.00331.x.  
 Stavrev P.Y. 2006. Inversion of elongated magnetic anomalies using magnitude transforms. *Geophysical Prospecting* 54, 153–166. doi:10.1111/j.1365-2478.2006.00550.x.

Strakhov V.N. 1970a. Some aspects of the plane inverse problem of magnetic potential. *Izvestiya Akademii Nauk SSSR Fizika Zemli* **9**, 31–41 (in Russian).

Strakhov V.N. 1970b. Some aspects of the plane gravitational problem. *Izvestiya Akademii Nauk SSSR Fizika Zemli* **12**, 32–44 (in Russian).

Thompson D.T. 1982. EULDPH: A new technique for making computer assisted depth estimates from magnetic data. *Geophysics* **47**, 31–37. doi:10.1190/1.1441278.

Zhdanov M.S. 1988. *Integral Transforms in Geophysics*. Springer-Verlag.

Zhdanov M.S. 2002. *Geophysical Inverse Theory and Regularization Problems*. Elsevier.

Zhdanov M.S. 2009a. *Geophysical Electromagnetic Theory and Methods*. Elsevier.

Zhdanov M.S. 2009b. New advances in 3D regularized inversion of gravity and electromagnetic data. *Geophysical Prospecting* **57**, 463–478. doi:10.1111/j.1365-2478.2008.00763.x.

Zhdanov M.S., Ellis R.G. and Mukherjee S. 2004. Regularized focusing inversion of 3D gravity tensor data. *Geophysics* **69**, 925–937. doi:10.1190/1.1778236.

Zhdanov M.S., Liu X. and Wilson G. 2010. Potential field migration for rapid 3D imaging of entire gravity gradiometry surveys. *First Break* **28**, 47–51.

**APPENDIX A: PHYSICAL INTERPRETATION OF THE ADJOINT GRAVITY GRADIENT OPERATOR**

Let us analyse the result of the adjoint gravity gradient operator applied to the observed gravity gradient field,  $A_T^* g_T$ . According to equation (12), we have:

$$A_T^* g_T = -2\gamma \int_L \frac{g_T^*(\zeta')}{(\zeta - \zeta')^2} d\zeta'. \tag{A1}$$

In particular, if the data are collected on the horizontal axis,  $z' = 0$ , equation (A1) takes the following form:

$$A_T^* g_T = -2\gamma \int_L \frac{g_T^*(\zeta')}{(\zeta - x')^2} dx'. \tag{A2}$$

We shall analyse more carefully the physical meaning of this equation. First of all, let us examine the expression for  $g_T^*(\zeta')$ . According to equation (10), we can write:

$$\begin{aligned} g_T^*(x') &= -2\gamma \iint_{\Gamma} \frac{1}{(\zeta^* - x')^2} \rho(\zeta) ds \\ &= -2\gamma \iint_{\Gamma^*} \frac{1}{(\zeta - x')^2} \rho(\zeta^*) ds = g_{T^*}(x'), \end{aligned} \tag{A3}$$

where  $g_{T^*}(x')$  can be treated as the gravity field of the masses located in domain  $\Gamma^*$ , which is a mirror image of domain  $\Gamma$  with respect to the real axis  $x$  (see Fig. A1).

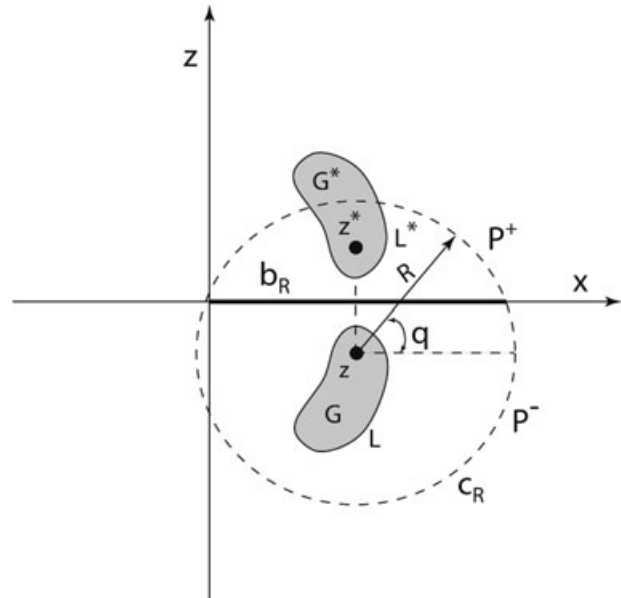


**Figure A1** Definition of the adjoint gravity gradient field  $g_{T^*}$ . The field  $g_{T^*}$  is generated by the sources located in  $\Gamma^*$ . The density distribution  $\tilde{\rho}(\zeta)$  within  $\Gamma^*$  is a mirror image of the density distribution  $\rho(\zeta)$  in  $\Gamma$ :  $\tilde{\rho}(\zeta) = \rho(\zeta^*)$ .

We will call this field,  $g_{T^*}$ , an *adjoint gravity gradient field*. The density distribution  $\tilde{\rho}(\zeta)$  within  $\Gamma^*$  is a mirror image of the density distribution  $\rho(\zeta)$  in  $\Gamma$ :  $\tilde{\rho}(\zeta) = \rho(\zeta^*)$ . Obviously, the field  $g_{T^*}$  of the sources located above the line of observation  $b$  (coinciding with the real axis  $x$ ) is an analytical function everywhere in the lower half-plane. It can be expressed in equivalent form as:

$$g_{T^*}(\zeta) = -2\gamma \iint_{\Gamma^*} \frac{1}{(\tilde{\zeta} - \zeta)^2} \tilde{\rho}(\tilde{\zeta}) d\tilde{s}, \quad \zeta \notin \Gamma^*, \quad z < 0, \tag{A4}$$

where  $\tilde{\zeta} = \tilde{x} + i\tilde{z} \in \Gamma^*$  is a variable of integration, and  $d\tilde{s} = d\tilde{x}d\tilde{z}$ .

Now we examine the expression  $A_T^* g_T$  in equation (A2). Let  $P^+$  stand for the upper half-plane of a complex plane  $\zeta$ , bounded by the real axis  $x$  and  $P^-$  for the lower half-plane. We consider an arbitrary point  $\zeta \in \Gamma$  and draw therefrom a circle of radius  $R$ . This part of the real axis  $x$  that happens to lie inside the circle will be represented by  $b_R$ , while the part of the circle found inside  $P^-$  will be denoted by  $C_R$  (see Fig. A1). By virtue of the Cauchy integral formula (Zhdanov 1988):

$$g_{T^*}(\zeta) = \frac{1}{2\pi i} \int_{b_R} \frac{g_{T^*}(\tilde{\zeta})}{\tilde{\zeta} - \zeta} d\tilde{\zeta} + \frac{1}{2\pi i} \int_{C_R} \frac{g_{T^*}(\tilde{\zeta})}{\tilde{\zeta} - \zeta} d\tilde{\zeta}, \tag{A5}$$

where the integration over the closed contour  $b_R \cup C_R$  is taken in the counter-clockwise direction. In particular, the

integration over the segment  $b_R$  of the real axis is from right to left. Let us now proceed to the limit as  $R \rightarrow \infty$ . The integral taken over the part of the circle  $C_R$  is written, upon substitution of the variable  $\tilde{\zeta} = \zeta + Re^{i\theta}$ , in the form:

$$\frac{1}{2\pi i} \int_{C_R} \frac{g_{T^*}(\tilde{\zeta})}{\tilde{\zeta} - \zeta} d\tilde{\zeta} = \frac{1}{2\pi} \int_{C_R} g_{T^*}(\zeta + Re^{i\theta}) d\theta. \quad (\text{A6})$$

Being analytic, the function  $g_{T^*}(\zeta)$  tends uniformly over  $\theta$  to zero at infinity, hence the limit of integral (A6) is zero. The integral along  $b_R$  as  $R \rightarrow \infty$  tends to the integral taken over the entire real axis  $x$ . Thus, in the limit, equation (A5) takes the form:

$$g_{T^*}(\zeta) = -\frac{1}{2\pi i} \int_{-\infty}^{\infty} \frac{g_{T^*}(\tilde{x})}{\tilde{x} - \zeta} d\tilde{x}, \quad \zeta \in P^-, \quad (\text{A7})$$

where the minus sign arises because we have changed the direction of the integration; it is now conducted from the left ( $-\infty$ ) to the right ( $+\infty$ ). Note that from equation (A3), it follows that, on the real axis,  $x$ :

$$g_T^*(\tilde{x}) = g_{T^*}(\tilde{x}). \quad (\text{A8})$$

Substituting equation (A8) into equation (A7), we find:

$$g_{T^*}(\zeta) = -\frac{1}{2\pi i} \int_{-\infty}^{\infty} \frac{g_T^*(\tilde{x})}{\tilde{x} - \zeta} d\tilde{x}, \quad \zeta \in P^-. \quad (\text{A9})$$

Taking into account equation (A9), we can rewrite equation (A2) as follows:

$$\begin{aligned} A_T^* g_T &= -2\gamma \int_{-\infty}^{\infty} \frac{g_T^*(\zeta')}{(\zeta - x')^2} dx' = 2\gamma \frac{\partial}{\partial \zeta} \int_{-\infty}^{\infty} \frac{g_T^*(\zeta')}{(\zeta - x')} dx' \\ &= 2\gamma \frac{2\pi i}{2\pi i} \frac{\partial}{\partial \zeta} \int_{-\infty}^{\infty} \frac{g_T^*(x')}{(\zeta - x')} dx' = -4\pi\gamma i \frac{\partial}{\partial \zeta} g_{T^*}(\zeta). \end{aligned} \quad (\text{A10})$$

Thus, we see that the application of the adjoint operator to the observed gravity gradient field,  $g_T$ , is equivalent to taking a derivative of the downward continuation of the adjoint gravity gradient field,  $g_{T^*}$ . Taking into account that, on the real axis  $x$ , the complex conjugate of the observed field is equal to the adjoint field (equation (A8)), we conclude that the adjoint gravity gradient operator is equivalent to the derivative of the downward continuation of the complex conjugate of the observed gravity gradient field.

## APPENDIX B: INTEGRATED SENSITIVITY OF THE COMPLEX INTENSITY OF THE GRAVITY GRADIENT FIELD

The integrated sensitivity of the complex intensity gravity gradient field is calculated by the following formula (Zhdanov 2002):

$$S_T = \frac{\|\delta g_T\|_D}{\delta\rho}, \quad (\text{B1})$$

where  $\delta g_T$  is the perturbation of the gravity gradient field resulting from a local perturbation of the density,  $\delta\rho(\zeta) = \rho(\zeta)ds$ , within a differential element of area  $ds$ , located at the point  $\xi = x + iz$  of the lower half-plane ( $z < 0$ ):

$$\delta g_T = \delta g_T(\zeta') = -2\gamma \frac{\rho(\zeta) ds}{(\zeta - \zeta')^2}. \quad (\text{B2})$$

Substituting equation (B2) into equation (B1), we find:

$$\begin{aligned} S_T &= \frac{1}{\rho(\zeta) ds} \sqrt{\int_L \delta g_T(\zeta') \delta g_T^*(\zeta') d\zeta'} \\ &= 2\gamma \sqrt{\int_L \frac{1}{|\zeta - \zeta'|^4} d\zeta'}, \end{aligned} \quad (\text{B3})$$

where  $L$  is some line of observations of the gravity gradients. In particular, if the profile of observations coincides with the horizontal axes  $x, z' = 0$ , the definite integral in equation (B3) can be calculated as:

$$\begin{aligned} S_T &= 2\gamma \sqrt{\int_{-\infty}^{\infty} \frac{1}{[(x - x')^2 + z^2]^2} dx'} \\ &= 2\gamma \sqrt{-\frac{1}{z^3} \int_{-\infty}^{\infty} \frac{1}{[\eta^2 + 1]^2} d\eta}, \end{aligned} \quad (\text{B4})$$

where the tabulated integral is given by:

$$\int_{-\infty}^{\infty} \frac{1}{[\eta^2 + 1]^2} d\eta = \frac{\pi}{2}. \quad (\text{B5})$$

Thus, we have:

$$S_T = 2\gamma \sqrt{\frac{1}{-z^3} \frac{\pi}{2}} = \gamma \sqrt{\frac{2\pi}{|z|^3}}, \quad z < 0. \quad (\text{B6})$$

Equation (B6) can be treated as the integrated sensitivity of the gravity gradient data to the local density anomaly located at the depth  $|z|$  in the lower half-plane ( $z < 0$ ). We can see that the sensitivity is inversely proportional to the square root of the cube of the depth of the density anomaly.